

# The separatrix operational space of ASDEX Upgrade due to interchange-drift-Alfvén turbulence

T. Eich<sup>1,\*</sup>, P. Manz<sup>1,2</sup> and the ASDEX Upgrade team<sup>a</sup>

<sup>1</sup> Max-Planck-Institute for Plasma Physics, Boltzmannstr. 2, D-85748 Garching, Germany

<sup>2</sup> Institute of Physics, University of Greifswald, Felix-Hausdorff-Str. 6, 17489 Greifswald, Germany

E-mail: [Thomas.Eich@ipp.mpg.de](mailto:Thomas.Eich@ipp.mpg.de) and [Peter.Manz@ipp.mpg.de](mailto:Peter.Manz@ipp.mpg.de)

Received 10 March 2021, revised 4 May 2021

Accepted for publication 21 May 2021

Published 8 July 2021



CrossMark

## Abstract

The efficient operation of a tokamak is limited by several constraints, such as the transition to high confinement or the density limits occurring in both confinement regimes. These particular boundaries of operation are derived in terms of a combination of dimensionless parameters describing interchange-drift-Alfvén turbulence without any free adjustable parameter. The derived boundaries describe the operational space at the separatrix of the ASDEX Upgrade tokamak, which is presented in terms of an electron density and temperature existence diagram. The derived density limits are compared against Greenwald scaling. The power threshold and role of ion heat flux for the transition to high confinement are discussed.

Keywords: turbulence, separatrix, tokamak, ASDEX Upgrade, density limit, L–H transition

(Some figures may appear in colour only in the online journal)

## 1. Introduction

The operational space for safe and efficient operation of a tokamak is limited by several constraints [1]. Of high interest is the Greenwald density limit for L-mode [2], accessibility of high confinement, H-mode [3] and loss of high confinement at about a Greenwald density fraction of unity [4–7]. The technically feasible operational range of tokamaks is also limited due to power exhaust requirements. The power exhaust capabilities of a magnetic confinement fusion device vastly depend on the plasma conditions around the separatrix [8, 9]. In previous work, we characterized the plasma conditions at the separatrix based on global turbulence parameters introduced by Rogers, Drake and Zeiler (RDZ) [10] and Scott [11]. In [12], an increase in the plasma decay lengths around the separatrix


was shown to be correlated with the turbulence parameter  $\alpha_t$  (see table 3 for definitions).

$$\alpha_t = 3.13 \times 10^{-18} R_{\text{geo}} \hat{q}_{\text{cyl}}^2 \frac{n_e}{T_e^2} Z_{\text{eff}}. \quad (1)$$

Here, we will present and derive three boundary lines describing the L–H (H–L) transition, L-mode density limit and ideal ballooning mode limit for the plasma edge ( $n_{e,\text{sep}} - T_{e,\text{sep}}$ ) space just inside the separatrix. The presented model equations have been developed on the basis of a dedicated and carefully established experimental database in conjunction with heuristic techniques to derive these equations from the complex drift-Alfvén (DALF) model. This heuristic approach does not guarantee an optimal, complete or self-consistent solution. Trial and error has been one of our major approaches. It is the finally accomplished agreement to the experimental data justifying our ansatz. Characteristic wavenumbers of DALF turbulence will be key quantities in this study. These are summarized in table 1. Their derivation is found in the appendix A. All quantities entering the definitions of the characteristic wavenumbers are summarized in table 2. Fundamental plasma and discharge parameters are summarized in table 3.

<sup>a</sup> See Meyer *et al* 2019 (<https://doi.org/10.1088/1741-4326/ab18b8>) for the ASDEX Upgrade Team.

\* Author to whom any correspondence should be addressed.

 Original content from this work may be used under the terms of the [Creative Commons Attribution 3.0 licence](https://creativecommons.org/licenses/by/3.0/). Any further distribution of this work must maintain attribution to the author(s) and the title of the work, journal citation and DOI.

**Table 1.** Characteristic perpendicular wavenumbers normalized to  $\rho_s$ .

$k_{EM}$	$k_{RBM}$	$k_{ideal}$
$\sqrt{\beta_e/\mu}$	$k_{\parallel}/\sqrt{(1+\tau_i)C\sqrt{\omega_B}}$	$\sqrt{\beta_e\sqrt{\omega_B}/C}(q_s R/\lambda_{\perp})$

**Table 2.** Characteristic quantities of DALF turbulence.

$\rho_s$	$\sqrt{T_e m_i}/eB$
$c_s$	$\sqrt{T_e/m_i}$
$\mu$	$m_e/m_i$
$\tau_i$	$T_i/T_e$
$\beta_e$	$\mu_0 n_e T_e/B^2$
$\omega_B$	$2\lambda_{\perp}/R$
$C$	$0.51\mu\nu_{ei}(q_s R)^2/(c_s\lambda_{\perp})$
$\alpha_t$	$(1+\tau_i)C\omega_B$
$\alpha_d$	$2^{-\frac{1}{4}}\pi^{-1}\omega_B^{\frac{1}{4}}\alpha_t^{-\frac{1}{2}}$

The paper is organized as follows: in order to structure our paper for good readability, we start with the final product of our work, which is the separatrix operational space for ASDEX Upgrade and which is presented in section 2. Here, the database is introduced. Detailed comparisons of the derived boundaries with the experimental data set are given in section 3 for the L-mode density limit, in section 4 for the L–H (H–L) transition and in section 5 for the H-mode density limit. Derivations of the boundaries as well as detailed comparisons to previous work are given in appendix A.

## 2. Operational space of ASDEX Upgrade at the separatrix

In the following, the separatrix operational space of the ASDEX Upgrade tokamak in terms of density and electron temperature is illustrated. All presented data are estimated from plasma discharges with a mean plasma current  $I_p$  of about 0.83 MA and toroidal field strength  $B$  of about 2.5 T. These conditions provide a well-established operational regime in ASDEX Upgrade. Important here is that machine safety allows us to provoke the L-mode density limit either by gas puffing or through an H–L back transition at high densities. The experimental database has been obtained by edge Thomson scattering (TS) and need to be averaged for about 300 ms to give meaningful results. This requires dedicated discharges which are naturally limited in number. The use of TS allows us to monitor the entire operational range including the disruptive events that eventually occur at the L-mode density limit. Overall, 123 discharges are presented containing 1884 data points including the database presented in [12] at  $I_p = 0.83$  MA and  $B_{tor} = 2.5$  T. The reader is referred to this source for further details on the profile analysis, e.g. removal of type-I edge localized mode (ELM) time windows. All data use deuterium as the main species and favorable field direction in lower single-null configuration. Discharges with impurity seeding are not included as an accurate estimation of  $Z_{eff}$  at

the separatrix is not available. The value for  $Z_{eff}$  is set to  $1.24 \pm 0.13$  (see appendix J). Table 4 summarizes some selected plasma discharge parameters. These are the plasma current  $I_p$ , toroidal magnetic field strength  $B_{tor}$ , cylindrical safety factor  $\hat{q}_{cyl}$ , heating power crossing the separatrix  $P_{sep}$ , heating power  $P_{heat}$ , Greenwald fraction  $f_{GW}$ , plasma elongation  $\kappa_{geo}$  and triangularity  $\delta_{geo}$ . The cylindrical safety factor is defined in appendix K. The minor radius,  $a_{geo}$ , of ASDEX Upgrade is about 0.5 m and the major radius,  $R_{geo}$ , about 1.65 m.

Figure 1 shows measured pairs of separatrix electron density and temperature. All figures throughout the L-mode data are marked with circles ( $\circ$ ) and H-mode data with rectangles ( $\square$ ). Data points at the disruptive L-mode density limit are indicated by ( $\triangleleft$ ). When a disruptive L-mode density limit is detected after a back transition to L-mode conditions, ( $\star$ ) is used. The time interval of the discharge exposing L-mode conditions after an H–L back transition are differently marked for clarity by using diamonds ( $\diamond$ ). The data from different regimes are separated by three boundaries due to the turbulence properties discussed in this paper. These three boundaries describe the L–H (H–L) transition, L-mode density limit and ideal ballooning mode limit in H-mode. Together, they establish a separatrix operational space of the ASDEX Upgrade tokamak in terms of density and electron temperature.

The three lines are constructed by seeking the solution of equations (3), (8) and (12) by simply testing a range of electron temperatures (25–150 eV) for each density value. For this purpose, the ASDEX Upgrade scaling law for the electron pressure decay length (see [12]) is used. In addition, typical discharge parameters are set for elongation, triangularity, minor and major radius. To draw the lines, a plasma current,  $I_p$  of 831 kA and the toroidal magnetic field  $B_{tor}$  of 2.47 T have been used. These values correspond to the mean values of the 123 discharges presented. The variation in the boundary lines w.r.t. toroidal magnetic field, plasma current, plasma elongation and triangularity, as present in the database, is drawn as vertical lines. It should be noted that the presented data in the following sections (figures 2, 3 and 6) are calculated straight from the measured electron pressure decay lengths, exact geometries and all other discharge parameters.

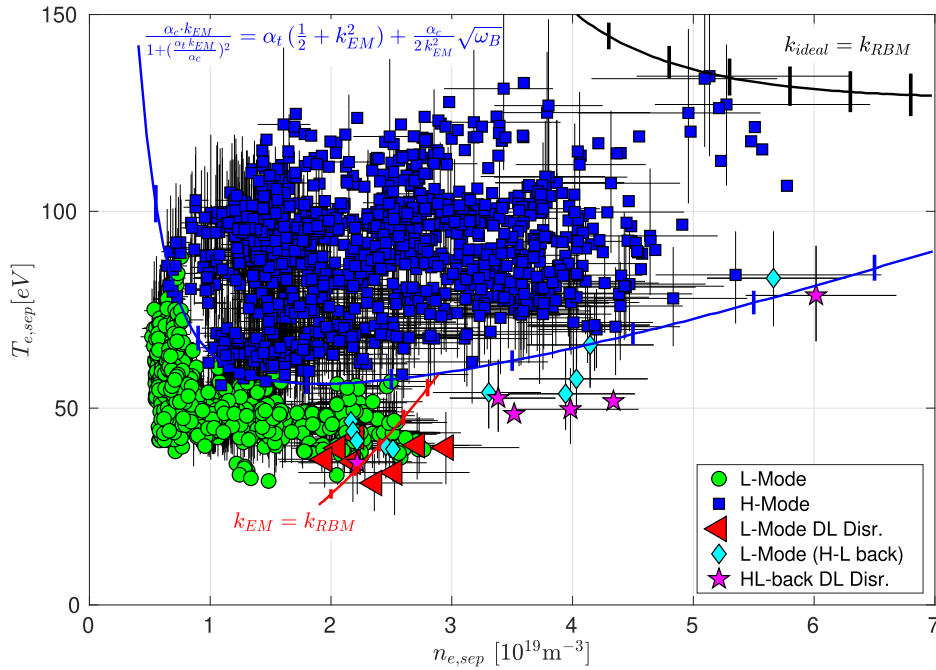
Operation in the low-confinement regime is clearly separated from operation in the high-confinement regime (blue line, equation (8)) in the  $n_{e,sep} - T_{e,sep}$  diagram. At low densities, the critical electron temperature for the L–H transition decreases with increasing density and vice versa for high densities. In L-mode, the accessible density is limited by a transition from electrostatic to electromagnetic resistive ballooning mode (RBM) turbulence (red line, equation (3)) and described in section 3. In H-mode, clearly higher densities can be achieved at the separatrix. Operation under high-confinement conditions is restricted at high temperatures and densities by ideal magnetohydrodynamic (MHD) (black line, equation (12)). At lower temperatures, back transition to L-mode occurs, which is stable only when the transition is below the RBM condition.

**Table 3.** Fundamental plasma and discharge parameters entering the definitions to characterize DALF turbulence.

Symbol	Unit	Selected as	
$T_{e/i}$	eV		Electron/ion temperature
$m_{e/i}$	kg		Electron/ion mass
$Z_{\text{eff}}$			Effective charge
$B$	T		Magnetic field strength
$n_e$	$\text{m}^{-3}$		Electron density
$\nu_{ei}$	1 s		Electron–ion collision frequency
$R$	m	$R_{\text{geo}}$	Major radius
$a$	m	$a_{\text{geo}}$	Minor radius
$\lambda_{\perp}$	m	$\lambda_{\text{pe}}$	Typical perpendicular length (equation (K.1))
$k_{\parallel}$	$1/q_s R$	$\sqrt{\alpha_c}$	Typical parallel wavenumber (equation (K.5))
$q_s$		$\hat{q}_{\text{cyl}}$	Safety factor (equation (K.6))

**Table 4.** Discharge parameters of analyzed L-mode and H-mode plasmas.

$I_p$ (MA)	$B_{\text{tor}}$ (T)	$\hat{q}_{\text{cyl}}$	$P_{\text{sep}}$ (MW)	$P_{\text{heat}}$ (MW)	$f_{\text{GW}}$	$\kappa_{\text{geo}}$	$\delta_{\text{geo}}$
0.83–0.84	2.38–2.56	3.8–5.4	0.3–14	0.4–16	0.2–1.0	1.5–1.8	0.16–0.33

**Figure 1.** Separatrix operational space of ASDEX Upgrade in terms of electron density and temperature. Different operation regimes are indicated by different symbols. Red line shows boundary of the L-mode density limit (equation (3)). Blue line indicates the L–H–L transition (equation (8)). Black line indicates the ideal MHD boundary (equation (12)). Error bars are plotted only for a subset of the data for clarity in the figure.

### 3. L-Mode density limit

In this section, the boundary given by the L-mode density limit, as shown by the red line in figure 1, will be derived. The L-mode density limit has been observed already in the very beginning of tokamak operation. Greenwald codified the maximum achievable density in tokamaks for L-mode operation. The commonly agreed upon upper limit for the density is thus given by so-called Greenwald density limit and is expressed

as,

$$n_{\text{GW}} = \frac{I_p}{\pi a_{\text{geo}}^2} [10^{20} \text{ m}^{-3}], \quad (2)$$

with  $I_p$  given in MA and  $a_{\text{geo}}$  being the minor radius of the tokamak equilibrium. An important feature of the L-mode density limit is that plasmas reaching a Greenwald density fraction of unity are observed to disrupt, which imposes most serious constraints on tokamak operation [13].

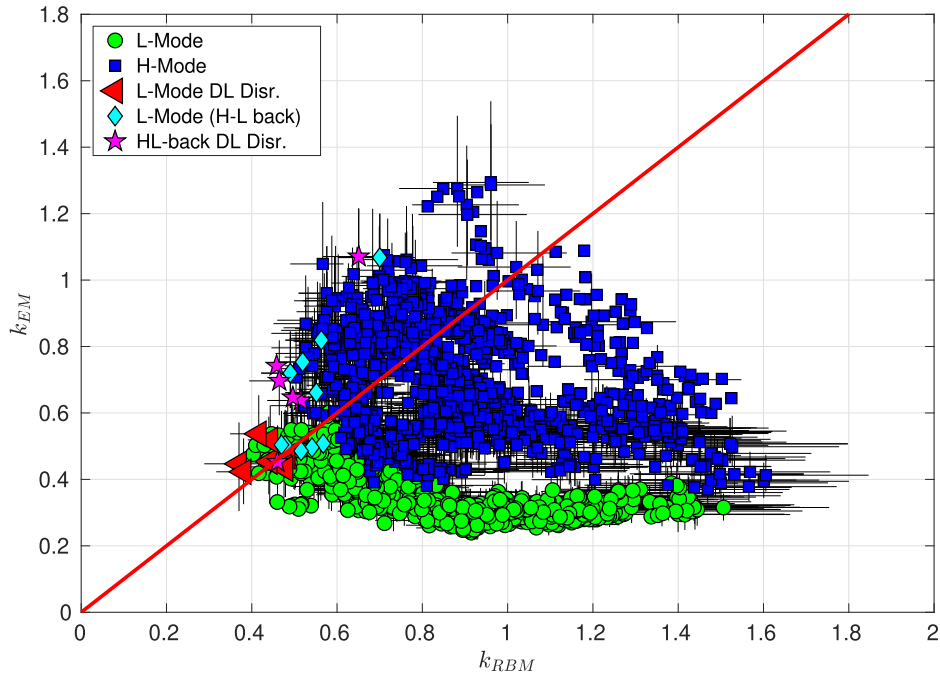


**Figure 2.** Characteristic electromagnetic wave number ( $k_{EM}$ ) against the characteristic wave number of the resistive ballooning mode ( $k_{RBM}$ ).

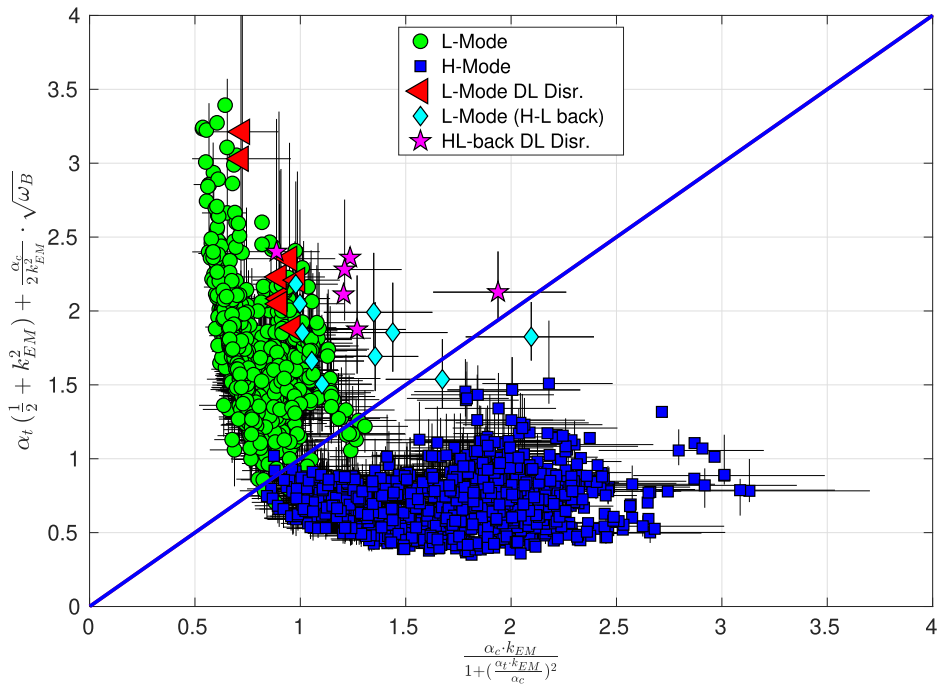


**Figure 3.** Stabilizing (abscissa) and destabilizing elements (ordinate) of condition 8. Blue line gives a 1:1 ratio and effectively acts as a distinction line for the confinement mode.

The density limit is a result of a sequence of events [14, 15]. It starts with radiative cooling of the edge, after which the multifaceted asymmetric radiation from the edge and MHD instabilities develop [15]. Finally, it ends with a disruption. A central question is which mechanism is initiating the cooling of the edge? Enhanced transport has been observed in advance of any change in the MHD activity in both experiments and numerical simulations when the Greenwald density

is approached [16–19]. A transition from the drift wave to the resistive ballooning regime induces a strong increase in turbulence transport. Approaching the density limit in ASDEX Upgrade L-mode conditions, turbulence is already in the regime of the RBM, as indicated by the values of the turbulence control parameters in [12]. Being in the RBM regime is not enough to trigger the density limit. An additional enhancement of the already strong turbulent transport is needed. As RBM

turbulence increases with increasing collisionality, a further increase in density leads to stronger transport. But at which point does turbulent transport gets catastrophically large? In [10], the strongly enhanced transport approaching the density limit has been ascribed to a further destabilization of the RBM by electromagnetic effects [20]. Also in [21], it has been found that magnetic induction effects can destabilize RBMs below marginal ideal stability.

The importance of electromagnetic effects depends on the considered scale (appendix D). The dynamic of sufficient large-scale structures is always electromagnetic. However, this does not necessarily imply that they drive strong transport. With increasing plasma beta the characteristic wave number, below which electromagnetic effects are important, shifts to higher wave numbers (appendix D). At some point the characteristic wave number of the RBM (appendix B) is within the wave number range of electromagnetic activity. This provides the condition that the scale of the RBM (equation (B.12)) is equal to the characteristic electromagnetic scale (equation (D.3)),

$$k_{\text{RBM}} = k_{\text{EM}}, \quad (3)$$

as the trigger condition for strongly enhanced transport. An increase in density is reflected both in the level of collisionality and plasma beta. Thus, the condition in equation (3) is in agreement with the increase in turbulent RBM-dominated transport by increasing collisionality triggering the density limit, as described in [19]. A more detailed discussion of the comparison of this condition 3 to the work by RDZ [10] is found in appendix F.

How this strongly enhanced transport finally leads to the chain of events of the L-mode density limit is not in the scope of this work. As the separatrix is in the RBM regime, strong filamentary activity can be expected. Due to the high divertor collisionality, the filaments are likely to be in the inertial regime of propagation [22]. Also with being in the electromagnetic regime, these filaments are similar to edge-localized-mode (ELM) filaments, even faster [23] and propagating deeper into the far scrape-off layer (SOL) and enhancing the plasma wall interaction. The resulting enhanced impurity source leads to cooling, likely first around the X-point. Enhanced conduction from the midplane to the X-point region leads to cooling at the outboard midplane, further enhancing this process.

Condition 3 is shown in figure 2 for the experimental database. The characteristic electromagnetic wave number is equal to the RBM wave number. These L-mode density limit disruptions are detected, explicitly when condition 3 is fulfilled. This condition describes all L-mode density limits achieved by gas puffing. Interestingly, it can be seen that H-mode discharges are not affected by this condition. However, plasmas falling back to L-mode also fulfill this condition and are observed to disrupt eventually. This effect is well illustrated in figure 1.

It is interesting to compare the separatrix density  $n_{e,\text{sep}}$  when equation (3) is fulfilled to the Greenwald density  $n_{\text{GW}}$ . Inserting the definitions for  $k_{\text{EM}}$  and  $k_{\text{RBM}}$  we have,

$$\frac{2\beta_c}{\mu} = \frac{\alpha_c}{\alpha_t} \sqrt{\omega_B}, \quad (4)$$

which is rewritten by assuming  $B_{\text{tor}}^2 \approx B^2$  as,

$$\frac{2\mu_0 n_{e,\text{sep}} T_{e,\text{sep}}}{\mu B_{\text{tor}}^2} = \frac{3.2 \times 10^{17} \cdot \alpha_c}{R_{\text{geo}} \hat{q}_{\text{cyl}}^2 \frac{n_{e,\text{sep}}}{T_{e,\text{sep}}} Z_{\text{eff}}} \sqrt{\frac{2\lambda_p}{R_{\text{geo}}}}. \quad (5)$$

Using,

$$\frac{B_{\text{tor}}}{\mu_0 R q_{\text{cyl}}} = \frac{I_p}{2\pi a^2 \hat{\kappa}^2} = \frac{1}{2 \times 10^{20}} \frac{n_{\text{GW}}}{\hat{\kappa}^2}, \quad (6)$$

we resolve for the Greenwald density fraction at the separatrix and find,

$$\frac{n_{e,\text{sep}}}{n_{\text{GW}}} = 0.11 \frac{\sqrt{\alpha_c}}{\hat{\kappa}^2} \sqrt{\frac{T_{e,\text{sep}}}{Z_{\text{eff}}}} \lambda_p^{\frac{1}{4}} R_{\text{geo}}^{\frac{1}{4}}. \quad (7)$$

Thus, condition 3 is written in terms of the Greenwald fraction. We note that  $\lambda_p$  itself depends on turbulent transport and in this way on the separatrix density. Thus, the ratio of  $n_{e,\text{sep}}$  and Greenwald density  $n_{\text{GW}}$  is not fully self-consistent. Inserting typical values in equation (7) just prior to the actual L-mode density limit, we calculate  $n_{e,\text{sep}}/n_{\text{GW}} = 0.21$  in accordance with the actual measured values of  $n_{e,\text{sep}}/n_{\text{GW}}$  ranging between 0.19–0.25 while the line-averaged Greenwald density fraction ranges between 0.51–0.63. These latter values are taken here for a typical L-Mode discharge at  $B_{\text{tor}} = 2.47$  T and  $I_p = 0.831$  MA,  $T_{e,\text{sep}} = 45$  eV,  $Z_{\text{eff}} = 1.24$ ,  $\alpha_c = 2.4$ ,  $\hat{\kappa} = 1.4$  and  $R_{\text{geo}} = 1.65$  m. The mean value for the pressure fall-off length just prior to the L-mode density limit in the database is about  $\lambda_p = 25$  mm, in line with previous measurements [24, 25].

It can be seen from equation (7) that the leading dependency for the separatrix density  $n_{e,\text{sep}}$  is the Greenwald density  $n_{\text{GW}}$ . Comparison of  $n_{e,\text{sep}}$  and the line-averaged density in conjunction with L-mode decay length studies [26] are needed to draw further conclusions. However, it can be seen that large values of  $Z_{\text{eff}}$  lead to lower density values, fairly modest dependence on geometry and weak dependence on heating power, as the square root of the separatrix temperature at high densities is described by  $\sqrt{T_{e,\text{sep}}} \approx P_{\text{sep}}^{\frac{1}{2}}$  [24, 25]. These latter findings are characteristic of the Greenwald density limit [4].

#### 4. Low to high confinement transition (L–H transition)

The lower boundary of efficient operation is the L–H transition shown by the blue line in figure 1. The main difference between L- and H-mode is the reduced level of turbulent transport in the H-mode compared to the L-mode. Turbulent transport can be suppressed by  $E \times B$  shear flows, which are particularly pronounced in H-mode. L–H transition occurs when turbulence collapses. This happens when the shear flow is sinking energy from turbulence faster than turbulence grows. As an approximation of the flow shear we take here the flow shear due to the neoclassical electric field, proportional to the gradient of the ion background pressure. This is the leading effect of stabilization in ASDEX Upgrade close to the L–H transition [27]. However, additional stabilizing effects were tested and selectively included to obtain better agreement with experimental

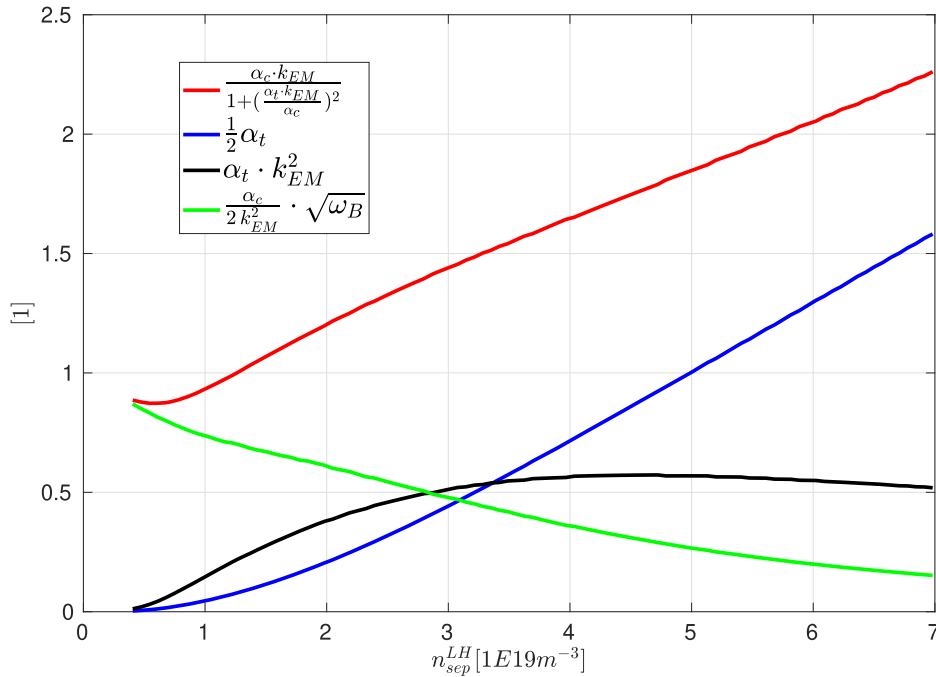


**Figure 4.** Individual dependence of the terms related to the effective turbulence suppression by flow shear ( $\alpha_c k_{EM}$ , red), effective turbulence growth of electron thermal turbulence ( $\frac{1}{2}\alpha_t$ , blue), kinetic turbulence ( $\alpha_t k_{EM}^2$ , black) and ion thermal turbulence ( $\frac{1}{2}\alpha_c k_{EM}^{-2} \sqrt{\omega_B}$ , green) on  $n_{e,sep}$  at the L- to H-mode transition.

observation. The included additional stabilization mechanisms are the so-called diamagnetic and beta stabilization. The turbulent field is divided into three parts, fluctuations in the electric field, electron and ion pressure. The distinction between the different fields is necessary since the interchange effect on the electron pressure fluctuations can be efficiently suppressed by the drift-wave mechanism, whereas ion temperature fluctuations cannot be compensated. Therefore, for the ion pressure fluctuations ideal interchange growth rates can be assumed corresponding to ion temperature gradient (ITG) turbulence. For the electron pressure fluctuations this is different. The stabilization by drift waves is called diamagnetic stabilization (see appendix E), which introduces a dependency on turbulence control parameter  $\alpha_t$ . Turbulence control parameter  $\alpha_t$  determines the cross-phase between plasma potential and electron pressure fluctuation, and thereby controls the turbulent transport. For L–H transition, diamagnetic stabilization is quite strong as turbulence close to the L–H transition occurs in the drift-wave dominated regime. In addition, the efficiency of the energy transfer between shear flow and turbulence depends on  $\alpha_t$ , which is taken into account. This effect is not very important for L–H transition occurring at low  $\alpha_t$ , but shows significant modification for H–L back transition. It is assumed that the turbulent transport is mainly electrostatic in stable L-mode plasmas [28–30]. We further assume that the largest electrostatic structures are the dominant ones for the turbulent transport and take  $k_{EM}$  as the characteristic perpendicular wavenumber. In this way, beta stabilization is taken into account and a dependency on the plasma beta is introduced. A detailed derivation of the L–H criterion (equation (H.10)) can be found in appendix H.

Ion temperature measurements at the separatrix are only available for isolated discharges and time windows of the database. Thus, ion and electron temperatures are assumed to be equal. Hence,  $\tau_i = \Lambda_{pi} = 1$ , and equation (H.10) is given by,

$$\frac{\alpha_c k_{EM}}{1 + \left(\frac{\alpha_t}{\alpha_c} k_{EM}\right)^2} > \alpha_t \left(\frac{1}{2} + k_{EM}^2\right) + \frac{1}{2} \frac{\alpha_c}{k_{EM}^2} \sqrt{\omega_B}. \quad (8)$$

Figure 3 shows the stabilizing effect related to the energy transfer into the shear flow on the abscissa and the destabilizing effect of turbulence growth related to the electron free energy, kinetic energy and ion free energy on the ordinate. Discharges in the low-confinement regime show pronounced destabilizing influences. The term  $\alpha_t \left(\frac{1}{2} + k_{EM}^2\right) + \frac{1}{2} \frac{\alpha_c}{k_{EM}^2} \sqrt{\omega_B}$  frequently exceeds one and approaches values up to three, while the term  $\alpha_c k_{EM}$  hardly exceeds one but often appears below one. On the other hand, the discharges in the high-confinement regime show much stronger stabilizing effects. The term  $\alpha_c k_{EM} / (1 + ((\alpha_t / \alpha_c) k_{EM})^2)$  is usually above one and approaches values of up to five. The transition from L- to H-mode appears somewhere close to the (blue) 1:1 line in figure 3, which describes condition 8. Therefore, condition 8 is fulfilled within the error bars of the measurements. Seeking the electron temperature for the plotted range of  $n_{e,sep}$  values in figure 1 to fulfill equation (8) then gives the blue line.

We have a closer look at the individual contributions to turbulence at the L–H transition. This is shown in figure 4 in dependence of the separatrix density. Note that L–H transitions can only appear in ASDEX Upgrade for separatrix densities of less than  $n_{sep}^{LH} = 2.7 \times 10^{19} \text{ m}^{-3}$  (figure 1) for the

given field and current ( $I_p = 0.83$  MA,  $B_{\text{tor}} = 2.4\text{--}2.6$  T). In this range, the ion channel  $\frac{1}{2} \frac{\alpha_c}{k_{\text{EM}}^2} \sqrt{\omega_B}$  is the most relevant one, which has to be suppressed by the flow shear to trigger the L–H transition. In the most common discharge scenario, the separatrix density is very close to  $n_{\text{sep}}^{\text{LH}} \approx 1.0 \times 10^{19} \text{ m}^{-3}$ . Here, all contributions other than the ion channel can be neglected, which supports the importance of the ion heat flux [31, 32].

Turbulence suppression balances the ion thermal turbulence channel, which is also due to the  $\alpha_c$  dependence of both terms. For typical ASDEX Upgrade discharges,  $\alpha_c$  is significantly above one, which strengthens the capability to suppress turbulence ( $\alpha_c k_{\text{EM}}$ ). In addition, the relative importance of the ion thermal channel (proportional to  $\alpha_c$ ) compared to the electron channel (not proportional to  $\alpha_c$ ) increases. At reduced elongation (lower  $\alpha_c$ ) the relative importance of the electron to the ion channel increases and the shear suppression capabilities decrease.

At  $n_{\text{sep}}^{\text{LH}} \approx 3 \times 10^{19} \text{ m}^{-3}$ , all turbulence channels contribute equally and for high densities the electron channel is the most relevant one. Therefore, for the L–H transition the ion channel is the most relevant one. For H–L back transitions at high  $\alpha_i$  (high density) the electron channel is the most relevant one. In addition,  $\alpha_c k_{\text{EM}} / (1 + ((\alpha_i / \alpha_c) k_{\text{EM}})^2)$  increases less strongly for high densities. This is due to the influence of the denominator taking into account the efficiency of energy exchange between turbulence and flow shear. At low densities the energy exchange is very efficient and the denominator can be neglected. At high densities this effect can possibly trigger an H–L back transition.

#### 4.1. Comparison to L–H power threshold scaling laws

Rigorous comparison of the proposed mechanism for the L- to H-mode transition to the scaling by Martin [33] and estimates by Ryter [31] cannot be performed as all considerations here apply strictly to the separatrix domain. Martin scaling uses heating power and line-averaged density. The work by Ryter puts the ion energy fluxes at about 10 mm inside the separatrix in focus. In order to present a *sanity check* and to compare the mechanism to the total heating power and ion power crossing the very edge region, we proceed in the following way. We generate for different toroidal magnetic fields numerically the solutions of relation (8) and solve for the electron temperature,  $T_{\text{e,sep}}^{\text{LH}}$ , in dependence of the electron density, i.e. generating the *blue* graph of figure 1 for  $B_{\text{tor}} = 2.1, 2.3, 2.5$  and 2.7 T.

We use the model by Stangeby [34]:

$$T_{\text{e,sep}} \approx \left( \frac{7 P_{\text{sep}} \times L_c}{4 \kappa_0^c \cdot A_{\text{SOL}}} \right)^{\frac{2}{7}}. \quad (9)$$

The connection length,  $L_c$  from the outer mid-plane region to the divertor is  $L_c = \pi q_{\text{cyl}} R$ . The effective area,  $A_{\text{SOL}}$  is written as  $A_{\text{SOL}} = 4\pi R \lambda_q \frac{B_{\text{pol}}}{B_{\text{tor}}}$  with  $\lambda_q$  as the power fall-off length, which is approximated using  $\lambda_q = \frac{2}{7} \lambda_T$ . Using the effective elongation (see equation (K.7))  $\hat{k}$ , the aspect ratio  $A = R/a$ ,  $\hat{q}_{\text{cyl}}$  and with  $\kappa_0^c$  being Spitzer–Härm electron heat

conduction, we rewrite equation (9) as,

$$T_{\text{e,sep}} \approx \left( \frac{7 P_{\text{sep}} q_{\text{cyl}}^2 A}{16 \kappa_0^c \hat{k} \lambda_q} \right)^{\frac{2}{7}}. \quad (10)$$

From this, we calculate the electron heat flux at the L- to H-mode transition by inserting  $T_{\text{e,sep}}^{\text{LH}}$  according to,

$$P_{\text{sep,e}}^{\text{LH}} \approx \frac{16 \kappa_0^c \hat{k} \lambda_q a_{\text{geo}}}{7 \hat{q}_{\text{cyl}}^2 R_{\text{geo}}} \times (T_{\text{e,sep}}^{\text{LH}})^{\frac{7}{2}}. \quad (11)$$

The power associated with the electron heat flux crossing the separatrix is shown on the left-hand side of figure 5. This shows the typical non-monotonic density dependence at its typical minimum. On either side of this minimum, the critical power increases. These are called the low- and the high-density branches. At a typical toroidal magnetic field of 2.5 T, relation 8 predicts the minimum power at the local minimum to be about 700 kW at a separatrix density slightly above  $10^{19} \text{ m}^{-3}$ . Note that the separatrix density varies between 1/4 to 1/3 of the line-averaged density in this database at the L- to H-mode transition. The power increases with the magnetic field, as can be seen in figure 5. Thus, relation 8 recovers the behavior of the L–H power threshold in terms of density and magnetic field strength qualitatively. Quantitatively, good agreement is found for both total power as well as minimum density. However, the major radius dependence established in Martin scaling is not found by the estimated electron heat flux.

The ion heat flux at the L- to H-mode transition is calculated assuming the electron and ion temperature and their gradient to be equal around the separatrix. The latter assumption is certainly not a rigorous choice. However, we are interested in the basic parameter dependencies of the heating power and, in particular, its machine size dependence. The power crossing the separatrix associated to neoclassical ion heat flux is given by  $P_{\text{sep,i}}^{\text{LH}} = 2\pi \kappa a_{\text{geo}} 2\pi R_{\text{geo}} n_{\text{e,sep}} \chi_{\text{neo}} \frac{T_{\text{e,sep}}}{\lambda_T}$ . Ryter proposed a linear dependency of the ion heat flux required for the L- to H-mode transition on density [31]. The neoclassical thermal diffusivity  $\chi_{\text{neo}}$  is calculated according to Angioni and Sauter [35]. In the derivation of the neoclassical transport coefficients in [35] it has been assumed that the poloidal ion Larmor radius is small compared to the pressure gradient fall-off length  $\rho_{\text{i,pol}} \ll \lambda_p$ , which is only marginally fulfilled. The calculated neoclassical ion heat flux is shown in figure 5. For the typical density range of the L- to H-mode transition,  $n_{\text{e,sep}} = 1\text{--}3 \times 10^{19} \text{ m}^{-3}$ , an approximate linear relationship between ion heat flux and both density and toroidal field is found. Also of major importance is the linear dependence of the heat flux both with the major and the minor radius, which is absent for the electron heat flux. This supports the importance of the ion heat flux and thus is considered here to be an important link between the well-known power threshold dependency with the plasma surface area in Martin scaling and the approach by Ryter.

Finally, we check the consistency of our model with the well-established experimental findings of the radial electric field in ASDEX Upgrade. By using the electron density and temperature values at the L- to H-mode transition (given by

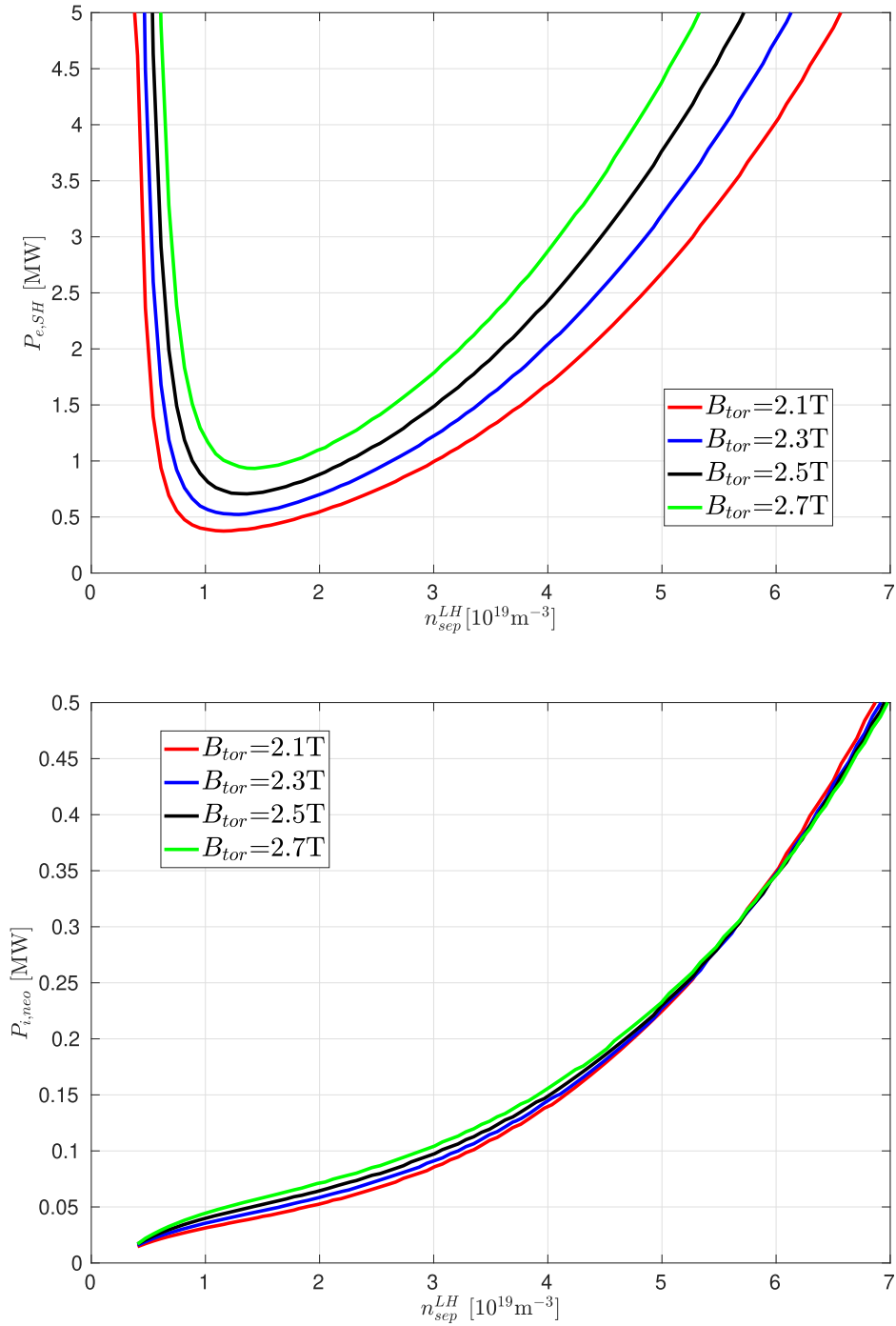


**Figure 5.** Power threshold for the L–H transition in the electron and ion channel. Different colors show different magnetic field strength.

condition 8) and their fall-off lengths, we calculate the radial electric field at the very edge of ADEX Upgrade in H-mode [36] as well as close to the L–H transition [27] by making use of  $E_r \approx \frac{\nabla p_i}{e Z_{\text{eff}} n_e} \approx \frac{T_i}{e Z_{\text{eff}}} \left( \frac{1}{\lambda_{T_i}} + \frac{1}{\lambda_{n_e}} \right)$ . We remind the reader that we have set  $\tau_i = 1$  so that we can further approximate  $E_r \approx \frac{T_e}{e Z_{\text{eff}}} \left( \frac{1}{\lambda_{T_e}} + \frac{1}{\lambda_{n_e}} \right)$ . Inserting typical values for  $n_{e,\text{sep}}$  at the L- to H-mode transition in ASDEX Upgrade ranging from  $1\text{--}1.5 \times 10^{19} \text{ m}^{-3}$  (see figure 1) we calculate an electric field

ranging from  $E_r = 6\text{--}12 \text{ kV m}^{-1}$ . The reference position is  $\lambda_p/2 = 2.5 \text{ mm}$  inside the confinement region. These latter values are in line with those found by direct measurements for the radial electric field at the L–H transition of about  $10 \text{ kV m}^{-1}$  at the radial position  $R = R_{\text{sep}} - 2.5 \text{ mm}$  ( $\rho = 0.995$ ) [37, 38]. This estimate here will only serve as an initial check. We need to gain more insight by using direct ion temperature profile measurements around the separatrix.



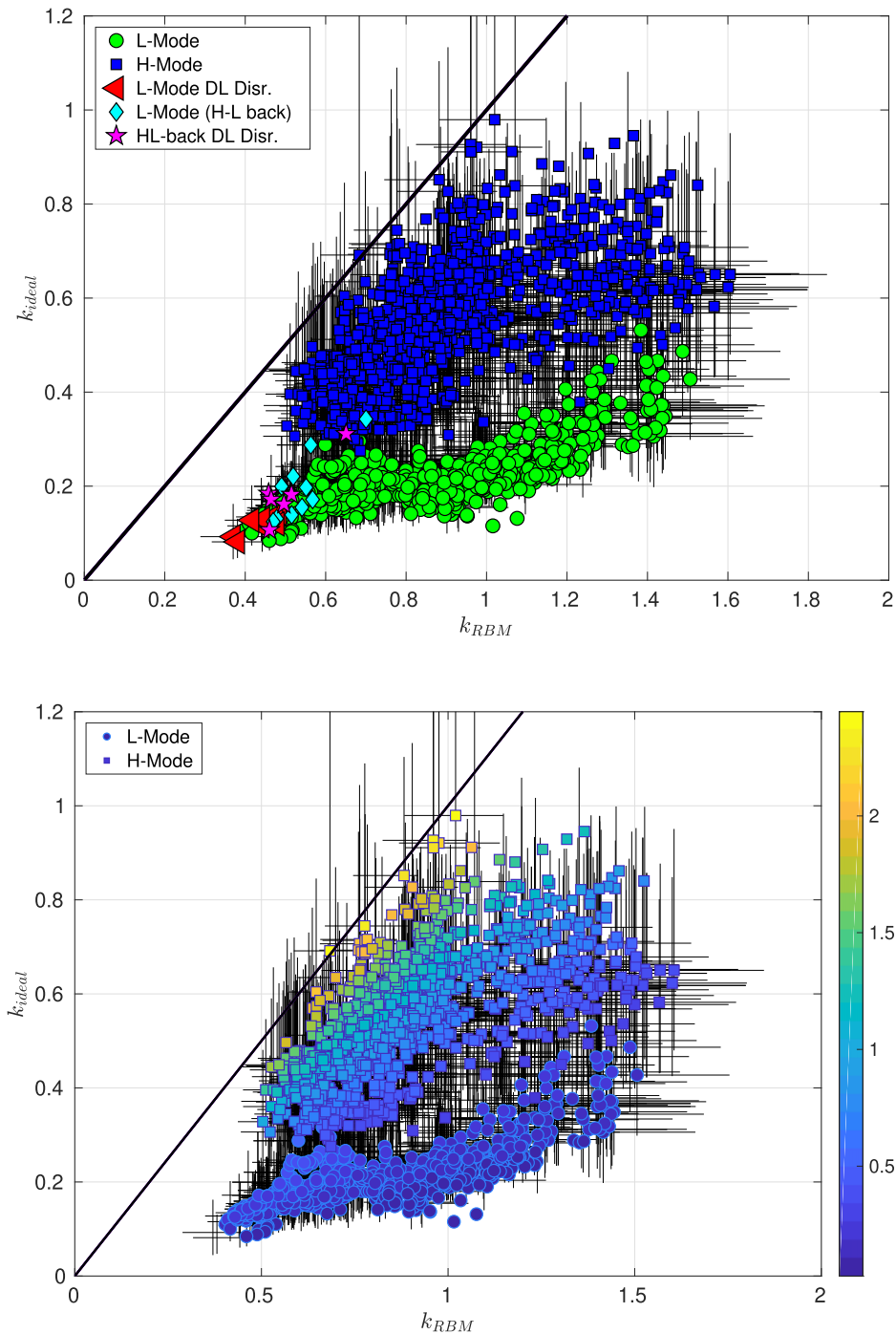


**Figure 6.** Comparison of the characteristic wavenumber  $k_{\text{ideal}}$  determining the boundary between resistive and ideal parallel dynamics and the characteristic wavenumber of the resistive ballooning mode  $k_{\text{RBM}}$ . Plot (a) shown with identical markers as in the other figures and (b) shown with color coding for  $\alpha_{\text{MHD}}$ .

## 5. Boundaries of H-mode operation at high densities

The boundaries occurring at high densities in the H-mode regime are discussed next. The limitation of H-mode operation at high densities is proposed to be the consequence of two distinct phenomena; first, an ideal-ballooning-mode limit and second, due to the loss of H-mode confinement properties. The loss of H-mode confinement properties is closely

related to the L–H transition, which was discussed in more detail in section 4. At high densities, however, transition to a stable L-mode is no longer possible and the condition of the L-mode density limit (section 3) sets in.

### 5.1. Ideal-ballooning-mode limit

The ideal-ballooning-mode limit is shown by the black line in figure 1. A condition of the transition from resistive to ideal

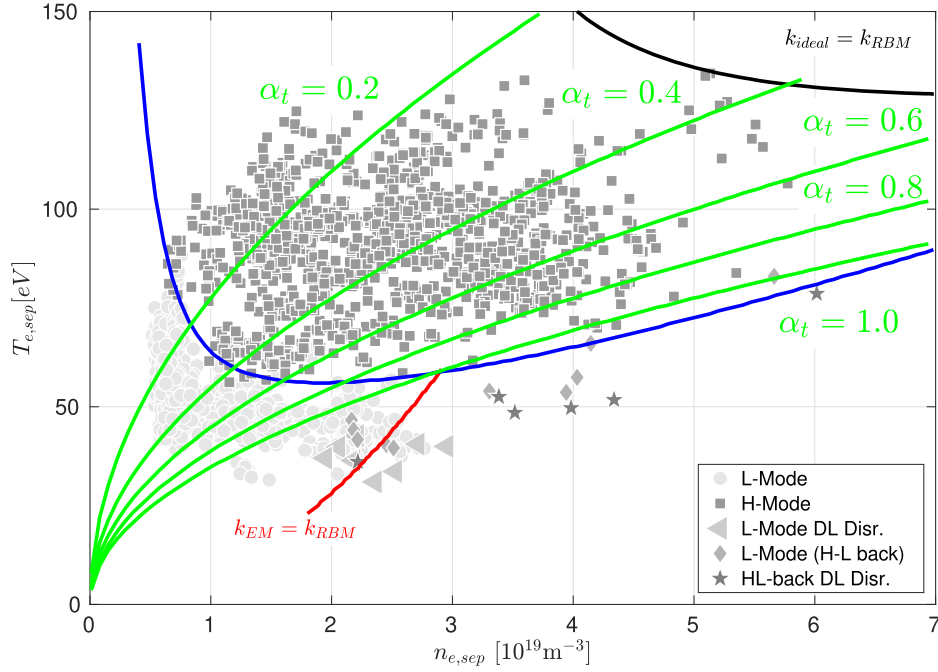


**Figure 7.** Separatrix operational space with isobars for  $\alpha_t = 0.2, 0.4, 0.6, 0.8, 1.0$ .

MHD is provided by,

$$k_{\text{ideal}} = k_{\text{RBM}}, \quad (12)$$

as derived in appendix G. In order to draw the latter criterion into the  $(n_{e,\text{sep}}, T_{e,\text{sep}})$  space, as shown in figure 1, i.e. construct the black line in the figure, we set  $p_{\text{sep}} = n_{\text{sep}} T_{\text{sep}} (1 + \tau_i)$  and insert  $\lambda_p$  from equation (K.1). If this condition is fulfilled, the separatrix becomes unstable to ideal MHD ballooning. For clarity, we note that the condition refers to the inter-ELM background quantities, which is different to ELMs appearing transiently.

Figure 6 shows the comparison between  $k_{\text{ideal}}$  and  $k_{\text{RBM}}$  using  $\alpha_{\text{MHD}}$  as the color of each datum point. The figure illustrates that the criterion of equality between  $k_{\text{ideal}}$  and  $k_{\text{RBM}}$  is identical to  $\alpha_{\text{MHD}} = \alpha_c$  and that actual experiments reach these highest  $\alpha_{\text{MHD}}$  values.

The boundary given by this ideal MHD limit is apparently not a continuation of the red line describing the L-mode density limit. Both limits occur at very different values of density and temperature, plasma beta, collisionality and thus turbulence occurs in different regimes. In order to also compare  $k_{\text{ideal}} = k_{\text{EM}}$  to Greenwald density, we write:

$$\begin{aligned} \alpha_{\text{MHD}} &= \frac{R_{\text{geo}} q_{\text{cyl}}^2 (1 + \tau_i) p_e}{\lambda_p B_{\text{tor}}^2 / (2\mu_0)} \\ &= \frac{4\mu_0 R_{\text{geo}} q_{\text{cyl}}^2 n_{\text{sep}} T_{\text{sep}}}{1.2(1 + 3.6\alpha_t^{1.9}) \rho_{s,\text{pol}} B_{\text{tor}}^2} = \alpha_c, \end{aligned} \quad (13)$$

and resolve for the Greenwald density fraction:

$$\frac{n_{e,\text{sep}}}{n_{\text{GW}}} = (1 + 3.6\alpha_t^{1.9}) \frac{1.35}{\sqrt{T_{e,\text{sep}}}} \frac{\alpha_c R_{\text{geo}}}{\hat{k}^2 a_{\text{geo}}}$$

$$\approx (1 + 3.6\alpha_t^{1.9}) \frac{5.5}{\sqrt{T_{e,\text{sep}}}}. \quad (14)$$

The latter equation shows that for high-heated, good confinement plasmas with high separatrix temperatures ( $T_{e,\text{sep}} \approx 125 \pm 25$  eV) and thus  $\alpha_t \rightarrow 0$ , the separatrix Greenwald density fraction will approach,

$$\frac{n_{e,\text{sep}}}{n_{\text{GW}}} \approx \frac{5.5}{\sqrt{T_{e,\text{sep}}}} (1 + 0) = \frac{5.5}{\sqrt{125 \pm 25 \text{ eV}}} = 0.49 \pm 0.05.$$

The result is in accordance with [39]. For values of  $\alpha_t$  larger than about 1/2, significantly higher densities than  $\frac{n_{e,\text{sep}}}{n_{\text{GW}}} \approx \frac{1}{2}$  at the separatrix should also be obtained. However, due to the correlation between  $\alpha_t$  and  $H_{98,y2}$  [12], consequently lower  $H_{98,y2}$  will be measured. This behavior, namely an onset of confinement degradation scaling with Greenwald density  $n_{\text{GW}}$  is qualitatively in line with studies on the confinement properties at high densities in various devices [5, 40–43]. These reported findings on the separatrix properties are consistent with similar studies both at DIII-D [44] and JET [45].

Figure 7 adds isobars for  $\alpha_t$  onto the separatrix operational space plot. Due to the high temperatures, H-modes are still at low collisionalities and turbulence is in the drift-wavedominated regime. Thus, for all data points,  $\alpha_t < 1$  is observed.

## 5.2. Disruptive limit at low temperatures in H-modes

Figure 7 shows that there is another boundary for H-modes appearing at high densities and limiting its operation range, given by the blue line and thus by the back transition from high to low confinement. At low densities, this boundary line describes both L–H and H–L transitions. At high densities,

however, back transition to a stable L-mode regime is not possible as this region is not accessible due to the L-mode density limit (red line in figure 7). After H–L back transition at high densities, the plasma is in a regime of strongly enhanced transport (the electromagnetic RBM regime) leading inevitably to a disruption if not avoided by active means [46]. As can be seen in figure 7, H–L transitions at high densities are also accompanied by the transition from the drift-wave regime of turbulence ( $\alpha_t < 1$ ) to the RBM regime of turbulence ( $\alpha_t > 1$ ). The H–L back transition at high densities initiates the same process as at the L-mode density limit. With respect to separatrix density and temperature, this happens at other values, since these values are determined by the H–L back transition. The observed high densities and temperatures are not directly accessible from the L-mode regime. The disruptive density limit after an H–L back transition is preceded by a collapse of shear flow. And this can be triggered by non-efficient zonal flow drive at low adiabaticity [47], as proposed in [48]. The effect of reduced zonal flow drive at low adiabaticity has been taken into account in the derivation of the L–H condition in appendix H.

This shows that the density limit is not a consequence of a single condition. There are actually three different limits attributed to a density increase at the separatrix.

## 6. Summary and conclusion

In the present contribution, the boundaries of tokamak operation are related to the competition between drift-wave and resistive ballooning turbulence. The three boundaries discussed in this work depend on the plasma current  $I_p$  and toroidal magnetic field on axis  $B_{\text{tor}}$ . Therefore, to draw these boundaries in the  $(n_{e,\text{sep}}, T_{e,\text{sep}})$  space, plasma current and magnetic field strength are kept constant.

(a) *L-mode density limit*: in the low-confinement regime, the operation is limited by a disruptive density limit, occurring at high densities and low temperatures and therefore at high collisionalities. At these parameters, turbulence can be expected to be in the regime of the RBM. Here, the turbulent transport is already quite high. An additional strong enhancement of turbulent transport can be induced if the electrostatic RBM transits to an electromagnetic RBM. This is described by condition 3. The model developed here (equation (3)) is basically in line with the picture developed by RDZ [10]. The L-mode density limit occurs at high density and low temperatures; hence the high collisionality. At this parameter, turbulence is in the resistive ballooning regime, not stabilized by drift waves (low  $\alpha_d$ ). By increasing the density,  $\alpha_{\text{MHD}}$  increases, which leads to enhanced electromagnetic contributions to the turbulent transport. A boundary relation  $\alpha_{\text{MHD}} \sim \alpha_d^2$ , as proposed by RDZ [10], is reproduced (F.2). All disruptive discharges are captured by condition 3 within experimental error bars.

(b) *High confinement operation*: the transition from low to high confinement occurs in the regime of drift-wave turbulence. Thus, turbulent transport is rather moderate in L-mode preceding an L–H transition. A transition to H-mode can be triggered, when the energy transfer rate into the shear flow exceeds the energy input rate into turbulence [49]. Similar to the Kim–Diamond model [50], where the interaction between turbulence and zonal flow is most important, here the interaction between turbulence and the mean flow is assumed to be dominant, as proposed from ASDEX Upgrade experiments [27]. However, this interaction is treated in a similar way to that described by zonal flow physics. Additional stabilization effects by cross-phase modifications (diamagnetic stabilization), and due to electromagnetic effects, are taken into account, as proposed by RDZ [10]. The corresponding condition is derived in equation (8), which is valid within the error bars in the ASDEX Upgrade data set. At this condition (equation (8)), the remaining electron heat flux shows typical non-monotonic density dependence including the typical minimum. The remaining neoclassical ion heat flux shows a linear dependency on the density, as can be seen in the experiment. Based on this finding, we conjecture that the ion heat flux is responsible for the major radius dependence of the heat flux threshold. This supports interpretation of the critical role of the ion heat flux for the L–H transition [31].

(c) *High-density operation for H-mode discharges and appearance of ideal ballooning-modes*: a fundamentally important property found in the separatrix operational space when comparing L-mode and H-mode operation, irrespective of the explanation, is the finding that much higher  $n_{e,\text{sep}}$  values are achieved in high-confinement operation. At very high densities in H-mode and at still comparably high values for  $T_{e,\text{sep}}$ , ideal ballooning sets a boundary well visible in the  $(n_{e,\text{sep}} - T_{e,\text{sep}})$  space. Due to the separatrix high temperature, H-mode is still at low collisionalities and turbulence is expected to still be in the drift-wave dominated regime.

A second boundary is the back transition to L-mode. When the density is above the L-mode density limit density value given by the red line, the back transition to L-mode conditions necessarily exposes the same termination as L-mode operation. A back transition below the L-mode density limit value does lead to a stable L-mode. These discharges are included in the database.

Between the ideal ballooning limit and the H–L back transition line there is a gap allowing for higher densities. However, these discharges are not observed. Whether the absence of discharges with  $n_{e,\text{sep}} \geq 5.5 \times 10^{19} \text{ m}^{-3}$  whilst being in H-mode condition is due to restricted fueling efficiency [51], due to an unrevealed further constrain from separatrix physics [52] or of an entirely different nature, is currently under investigation.

## Acknowledgments

This work has been carried out within the framework of the EUROfusion Consortium and has received funding from the Euratom research and training programme 2014–2018 and 2019–2020 under Grant Agreement No. 633053. The views and opinions expressed herein do not necessarily reflect those of the European Commission. The authors appreciate the valuable discussions with and support of C. Angioni, P. David, M. Faitsch, A. Kallenbach, H. Meyer, V. Naulin, U. Stroth, E. Wolfrum and H. Zohm.

## Appendix A. Drift-Alfvén (DALF) model

The DALF model [53–55] describes DALF turbulence in toroidal geometry and, therefore, also includes interchange and MHD instabilities. A variety of mechanisms of plasma turbulence in toroidal geometry relevant to the plasma edge can be understood by the DALF model. It consists of evolution equations for the vorticity  $\tilde{\Omega}$

$$\left(\frac{\partial}{\partial t} + \tilde{u}_E \times \nabla\right) \tilde{\Omega} = B \nabla_{\parallel} \frac{\tilde{J}_{\parallel}}{B} - (1 + \tau_i) \mathcal{K}(\tilde{p}_e), \quad (\text{A.1})$$

the electron pressure  $\tilde{p}_e$

$$\left(\frac{\partial}{\partial t} + \tilde{u}_E \times \nabla\right) \tilde{p}_e + \tilde{u}_E \nabla p_e = B \nabla_{\parallel} \frac{\tilde{J}_{\parallel} - \tilde{u}_{\parallel}}{B} + \mathcal{K}(\tilde{\phi} - \tilde{p}_e), \quad (\text{A.2})$$

the parallel current  $\tilde{J}_{\parallel}$

$$\hat{\beta} \frac{\partial}{\partial t} \tilde{A}_{\parallel} + \hat{\mu} \left(\frac{\partial}{\partial t} + \tilde{u}_E \times \nabla\right) \tilde{J}_{\parallel} = \nabla_{\parallel} (p_e + \tilde{p}_e - \tilde{\phi}) - C \tilde{J}_{\parallel}, \quad (\text{A.3})$$

and the ion velocity

$$\hat{\epsilon} \left(\frac{\partial}{\partial t} + \tilde{u}_E \times \nabla\right) \tilde{u}_{\parallel} = -(1 + \tau_i) \nabla_{\parallel} (p_e + \tilde{p}_e) + \mu_{\parallel} \nabla_{\parallel}^2 \tilde{u}_{\parallel}. \quad (\text{A.4})$$

The equations are completed by Ampere's law:

$$\tilde{J}_{\parallel} = -\nabla_{\perp}^2 \tilde{A}_{\parallel}, \quad (\text{A.5})$$

and polarization,

$$\tilde{\Omega} = \frac{1}{B^2} \nabla_{\perp}^2 (\tilde{\phi} + \tilde{p}_e). \quad (\text{A.6})$$

The times are normalized to  $\lambda_{\perp}/c_s$ , perpendicular spatial scales to the hybrid Larmor radius  $\rho_s = \sqrt{T_e m_i}/eB$  and parallel scales to  $q_s R$  with electron temperature  $T_e$ , ion mass  $m_i$ , magnetic field strength  $B$ , elementary charge  $e$ , safety factor  $q_s$  and major radius  $R$ . It should be noted that the ion sound speed  $c_s = \sqrt{T_e/m_i}$  used for normalization does not include the contribution of the ions. Their contribution is accounted for by  $\tau_i = T_i/\bar{Z}T_e$ , the ratio between ion and electron temperature. The average charge is  $\bar{Z} = n_e/\sum_j n_j$ , where  $j$  denotes the different ion species. Here,  $\lambda_{\perp}$  is the relevant gradient scale length, where we choose the electron pressure gradient length scale  $\lambda_{\perp} = -p_e/\partial_x p_e$ . The background pressure gradient is

given by  $p_e = -\Lambda_p x$  with  $\Lambda_p = \lambda_{\perp}/\lambda_{pe} = 1$ . The ion gradient length is taken into account by  $\Lambda_{pi} = \lambda_{pe}/\lambda_{pi}$ .

The turbulence is a result of the nonlinearity in the advective derivative included in the total time derivative  $d/dt = \partial/\partial t + u_E \cdot \nabla$  with  $E \times B$  velocity  $u_E$ . The main fluctuating quantities are the electrostatic potential  $\tilde{\phi} = e\phi/T_{e0}$  normalized to the background mean electron temperature  $T_{e0}$  and the electron pressure fluctuations normalized to a characteristic mean background pressure value  $p_{e0}$ . In addition, the fluctuations are normalized and given in units of  $\rho_s/\lambda_{\perp}$ , which is the smallness parameter. This is also the reason the times are normalized by  $\lambda_{\perp}/c_s$  in DALF and not by  $\rho_s/c_s$  as is more commonly done.

The coordinates can be expressed by  $(x, y, s)$ , where  $s$  is in the direction of the unperturbed magnetic field line and  $x$  and  $y$  are radial and binormal, respectively, locally perpendicular to the unperturbed magnetic field line. The curvature operator is given by,

$$\mathcal{K} = \omega_B (\sin s \partial_x + \cos s \partial_y), \quad (\text{A.7})$$

with  $\omega_B = 2\lambda_{\perp}/R$  and the curvature radius  $R$ , which is set to the major radius. The first contribution to the curvature is the geodesic curvature, the second the normal curvature.

Different regimes are set by the square of the parallel/perpendicular scale ratio  $\hat{\epsilon} = (q_s R/\lambda_{\perp})^2$ , where  $q_s$  is the safety factor and  $R$  the major radius, the normalized plasma beta given by  $\hat{\beta} = (4\pi n T_e/B^2)\hat{\epsilon}$  and the normalized mass ratio  $\hat{\mu} = (m_e/m_i)\hat{\epsilon}$ , which determine the relative transit Alfvén and electron thermal frequencies, respectively. The parallel current is dissipated by collisions represented by  $C = \hat{\mu}(0.51\nu_{ei}\lambda_{\perp}/c_s)$  with electron–ion collision frequency  $\nu_{ei}$ . The model includes an ion viscosity  $\mu_{\parallel}$ .

## Appendix B. Minimum resistive ballooning mode (RBM) model

The RBM takes its important role from the theory proposed by RDZ, where diamagnetic stabilization of RBM turbulence is key to the L–H transition. In addition, it is suggested that enhanced transport with increasing electromagnetic activity leads to the L-mode density limit. This provides motivation to derive the RBM in DALF. Pressure fluctuations are advected in the presence of a pressure gradient (equation (A.2)):

$$\frac{\partial}{\partial t} \tilde{p}_e + \tilde{u}_{Ex} \frac{\partial}{\partial x} p_e = 0. \quad (\text{B.1})$$

The perturbation is made unstable by the curvature at the bad curvature region ( $\cos s = 1$ ) of the tokamak. This leads to charge separation appearing in the vorticity equation (A.1):

$$\frac{\partial}{\partial t} \nabla_{\perp}^2 (1 + \tau_i) \tilde{\phi} = -(1 + \tau_i) \mathcal{K} \tilde{p}_e. \quad (\text{B.2})$$

We use the ansatz for a pure instability  $d/dt \rightarrow \gamma$ ,  $\nabla_{\perp} \rightarrow ik_{\perp}$ ,  $\mathcal{K} = ik_y \omega_B$  to obtain,

$$\gamma \tilde{p}_e = -ik_y \Lambda_{pe} \tilde{\phi}, \quad (\text{B.3})$$

and,

$$-\gamma k_{\perp}^2 \tilde{\phi} = -ik_y \omega_B \tilde{p}_e. \quad (\text{B.4})$$

We see that the phase between potential and electron pressure fluctuations are shifted by  $\pi/2$  (they are shifted by  $i$ ). Inserted into each other, this gives:

$$\gamma k_{\perp}^2 = \frac{k_y^2 \Lambda_{pe} \omega_B}{\gamma}.$$

If it is assumed that with  $k_{\perp} \approx k_y$  the ideal interchange growth rate is recovered:

$$\gamma_I = \sqrt{\omega_B \Lambda_{pe}}. \quad (\text{B.5})$$

By renormalization, this is equivalent to the well-known expression:

$$\gamma_I = c_s \sqrt{\frac{2}{R \lambda_{pe}}}. \quad (\text{B.6})$$

The ideal interchange instability provides a equal growth rate for all wave numbers. The resistivity in the parallel dynamics is used to define a selection on the perpendicular scale. In the vorticity equation (A.1), the charge separation by the curvature is balanced by the parallel current:

$$\nabla_{\parallel} \tilde{J}_{\parallel} = (1 + \tau_i) \mathcal{K} \tilde{p}_e, \quad (\text{B.7})$$

which gives,

$$ik_{\parallel} \tilde{J}_{\parallel} = i(1 + \tau_i) \omega_B k_y \tilde{p}_e. \quad (\text{B.8})$$

By inserting equation (B.3) into (B.8) and assuming that the growth rate can still be approximated by the ideal interchange instability  $\gamma_I$  (equation (B.5)),

$$ik_{\parallel} \tilde{J}_{\parallel} = (1 + \tau_i) \omega_B \Lambda_{pe} \frac{k_y^2}{\gamma_I} \tilde{\phi}. \quad (\text{B.9})$$

The resistivity determines the response of the potential to the parallel current perturbation in equation (A.3):

$$\nabla_{\parallel} \tilde{\phi} = -C \tilde{J}_{\parallel}, \quad (\text{B.10})$$

and hence,

$$\tilde{J}_{\parallel} = -i(k_{\parallel}/C) \tilde{\phi}. \quad (\text{B.11})$$

Inserted into equation (B.9) yields:

$$\frac{k_{\parallel}^2}{C} = (1 + \tau_i) \omega_B \Lambda_{pe} \frac{k_y^2}{\gamma_I}.$$

Inserting the ideal interchange growth rate (equation (B.5)) and solving for a characteristic perpendicular wavenumber,

$$k_{\text{RBM}} = k_{\parallel} / \sqrt{(1 + \tau_i) C \sqrt{\omega_B \Lambda_{pe}}}. \quad (\text{B.12})$$

This is in close agreement with the characteristic RBM scale previously estimated in [10, 20, 56, 57].

### Appendix C. Minimum ideal ballooning mode model

The MHD reduced vorticity equation (A.1) is given by,

$$\frac{d}{dt} \nabla_{\perp}^2 (1 + \tau_i) \tilde{\phi} = \nabla_{\parallel} \tilde{J}_{\parallel} - (1 + \tau_i) \mathcal{K} \tilde{p}_e. \quad (\text{C.1})$$

This includes the divergence of polarization and parallel currents important for fundamental MHD as well as the interchange effect important for the ballooning mode. With  $\frac{d}{dt} \rightarrow \gamma$ ,  $\nabla_{\parallel} \rightarrow ik_{\parallel}$ ,  $\nabla_{\perp} \rightarrow ik_{\perp}$ ,  $\mathcal{K} = i\omega_B k_y$  this can be written as,

$$-\gamma k_{\perp}^2 (1 + \tau_i) \tilde{\phi} = ik_{\parallel} \tilde{J}_{\parallel} - i(1 + \tau_i) \omega_B k_y \tilde{p}_e. \quad (\text{C.2})$$

For ideal MHD modes the induction determines the parallel dynamics (equation (A.3)):

$$J_{\parallel} = -\frac{ik_{\parallel} k_{\perp}^2}{\hat{\beta} \gamma} \tilde{\phi}. \quad (\text{C.3})$$

The evolution of the electron pressure is approximated as before (see equation (B.3)). Inserting equations (B.3) and (C.3) into (C.2) gives,

$$-\gamma (1 + \tau_i) k_{\perp}^2 = \frac{k_{\parallel}^2 k_{\perp}^2}{\hat{\beta} \gamma} - \frac{(1 + \tau_i) \omega_B \Lambda_{pe} k_y^2}{\gamma}.$$

Approximating  $k_{\perp} \approx k_y$  and multiplying by  $\gamma$ , the growth rate is given by [28],

$$\gamma^2 = \omega_B \Lambda_{pe} - \frac{k_{\parallel}^2}{(1 + \tau_i) \hat{\beta}}, \quad (\text{C.4})$$

which yields growth when positive, which is the case for the pressure gradient  $\Lambda_{pe}$  exceeding a certain critical gradient:

$$\alpha_{\text{MHD}} = (1 + \tau_i) \omega_B \Lambda_{pe} \hat{\beta} > k_{\parallel}^2 \equiv \alpha_c. \quad (\text{C.5})$$

This is the ideal MHD ballooning limit with  $\alpha_{\text{MHD}} = \frac{q_c^2 R \beta}{\lambda_{pe}}$  and  $\beta = (1 + \tau_i) \beta_e$ . Since the ideal ballooning mode does not depend on a perpendicular wavenumber, it will evolve on the largest scale possible in the domain. We identify the critical normalized gradient  $\alpha_c$  with the square of the characteristic parallel wavenumber. In circular geometry the critical normalized gradient is just the magnetic shear  $\alpha_c = 0.6 \hat{s}$ . To take into account effects from geometry in this work we approximate  $k_{\parallel}^2$  by the critical pressure gradient  $\alpha_c$ . In this way, we take geometric variations into account even though in a very rough approach.

### Appendix D. Electromagnetic regime

Electromagnetic fluctuations are a central element of the explanation of the L–H transition in the work by RDZ [10]. Electromagnetic fluctuations are induced by the first term in equation (A.3). To be efficient the induction has to be larger than other terms leading to dissipation. These are the second term (electron inertia) and last term (collisional dissipation). Considering an ideal plasma (collisionless), it is the electron inertia which has to be overcome:

$$\hat{\beta} \frac{\partial}{\partial t} \tilde{A}_{\parallel} > \hat{\mu} \frac{\partial}{\partial t} \tilde{J}_{\parallel}, \quad (\text{D.1})$$

due to Ampere's law (A.5)  $\tilde{A}_{\parallel} = \tilde{J}_{\parallel} / k_{\perp}^2$

$$\hat{\beta} \frac{\tilde{J}_{\parallel}}{k_{\perp}^2} > \hat{\mu} \tilde{J}_{\parallel}, \quad (\text{D.2})$$

which corresponds to a selection rule on the perpendicular scale [28, 29]:

$$k_{\perp}^2 < \frac{\hat{\beta}}{\mu} < \frac{2\beta_e}{\mu} \equiv (k_{EM})^2. \quad (D.3)$$

All wavenumbers below  $\beta_e/\mu$  (these are large modes) are electromagnetically active. Thus, tokamak edge turbulence is almost always in the electromagnetic regime. Condition (D.3) is here of central importance in the derivation of the L-mode density limit (section 3) as well as for the L–H transition (Sec. appendix H).

In H-mode conditions well above the L–H power threshold  $\beta_e \geq \mu$ , electromagnetic effects are important for all scales above the ion Larmor radius. Below this critical beta, the electromagnetic effects on transport are rather indirect [29] and the electrons become more non-adiabatic by magnetic induction. Non-adiabaticity leads to higher turbulent transport. However, it also introduces magnetic flutter stabilizing the dynamics [29]. If electromagnetic fluctuations lead to overall increased or decreased turbulent transport, this is not trivial and a result of a complex interplay of different fields and at different scales. Previous studies found the turbulent transport strongly increases with plasma beta [28, 58]. Only slightly below the critical beta  $\beta_e \lesssim \mu$  have stabilizing effects been found [59]. Close to the L–H transition, the plasma beta at the separatrix in ASDEX Upgrade is slightly below the critical beta ( $k_{EM} \approx 0.4 \lesssim 1$ , as can be seen in figure 2).

## Appendix E. Interchange-drift-wave competition

The strength of the turbulent transport is controlled by the cross-phase. This is because the interchange instability pressure and radial velocity fluctuations are in phase. In addition, the drift wave electron pressure and plasma potential fluctuations are in phase. The competition between the drift wave and interchange mechanism is determined mainly by the parallel dynamics as explained in the following. The actual competition between both mechanisms is balanced in the vorticity equation (A.1):

$$\frac{\partial}{\partial t}(1 + \tau_i)\nabla_{\perp}^2 \tilde{\phi} = \nabla_{\parallel} \tilde{J}_{\parallel} - (1 + \tau_i)\mathcal{K}\tilde{p}_e. \quad (E.1)$$

The curvature  $(1 + \tau_i)\mathcal{K}\tilde{p}_e$  leads to the interchange instability. The parallel response  $\nabla_{\parallel} \tilde{J}_{\parallel}$  stabilizes the interchange mode growth. As can be seen in the following, it is the resistivity that controls the efficiency of the stabilizing effect due to the parallel response. The electrostatic response of the parallel current is given by equation (A.3):

$$\tilde{J}_{\parallel} = \frac{ik_{\parallel}}{C}(\tilde{p}_e - \tilde{\phi}). \quad (E.2)$$

At low collisionality ( $C \rightarrow 0$ ) the parallel response is very efficient, at high collisionality ( $C \rightarrow \infty$ ) it is strongly hampered. By inserting the parallel current (equation (E.2)), a

linear analysis of equation (E.1) yields:

$$-i\omega k_{\perp}^2(1 + \tau_i)\tilde{\phi} = -\frac{k_{\parallel}^2}{C}(\tilde{p}_e - \tilde{\phi}) - i(1 + \tau_i)\omega_B k_y \tilde{p}_e.$$

From this it can be seen how electron pressure and plasma potential fluctuations are related:

$$\left(\frac{k_{\parallel}^2}{C} + i(1 + \tau_i)\omega_B\right)\tilde{p}_e = \left(\frac{k_{\parallel}^2}{C} + iC\omega k_{\perp}^2(1 + \tau_i)\right)\tilde{\phi},$$

or

$$\tilde{\phi} = \frac{k_{\parallel}^2 + i(1 + \tau_i)C\omega_B k_y}{k_{\parallel}^2 + i(1 + \tau_i)C\omega k_{\perp}^2}\tilde{p}_e. \quad (E.3)$$

For large modes (low  $k_{\perp}$ ) this can be simplified by neglecting the polarization current:

$$\tilde{\phi} = \left(1 + i(1 + \tau_i)C\omega_B \frac{k_y}{k_{\parallel}^2}\right)\tilde{p}_e. \quad (E.4)$$

In an  $i\delta$ -model, where,

$$\tilde{\phi} = (1 + i\delta_e)\tilde{p}_e, \quad (E.5)$$

the phase difference is given by,

$$\delta_e = (1 + \tau_i)C\omega_B \frac{k_y}{k_{\parallel}^2}. \quad (E.6)$$

The transition from a drift-wave dominated regime to a resistive interchange dominated regime occurs for typical scales ( $k_y \sim 1, k_{\parallel} \sim 1$ ) at  $(1 + \tau_i)C\omega_B = 1$ . In addition, the turbulent transport is mainly controlled by  $(1 + \tau_i)C\omega_B$ . The turbulent transport is:

$$\tilde{u}_{Ex}\tilde{p}_e = -ik_y\tilde{\phi}\tilde{p}_e = (1 + \tau_i)C\omega_B \frac{k_y}{k_{\parallel}^2}\tilde{p}_e^2. \quad (E.7)$$

For  $(1 + \tau_i)C\omega_B \ll 1$ ,  $\tilde{\phi} \approx \tilde{p}_e$  the turbulence is drift-wave dominated and the turbulent transport is low. For  $(1 + \tau_i)C\omega_B \gg 1$ ,  $\tilde{\phi} > \tilde{p}_e$  the turbulence is interchange dominated and the turbulent transport is high. This makes  $C\omega_B$  an important control parameter for electrostatic plasma edge turbulence. One can equally well consider the effect of  $(1 + \tau_i)C\omega_B$  as a destabilizing mechanism with respect to drift waves or as a stabilizing mechanism with respect to interchange modes. We define:

$$\alpha_t = (1 + \tau_i)C\omega_B, \quad (E.8)$$

as the turbulence control parameter.

RDZ [10] also recognized the competition between drift waves and RBMs. They introduced the so-called diamagnetic parameter:

$$\alpha_d = \frac{1}{2\pi q_s R} \sqrt{\frac{m_i}{m_e} \frac{c_s R}{0.51\nu_{ei}}} \left(\frac{R}{\lambda_p}\right)^{1/4}, \quad (E.9)$$

describing the stabilizing effect of driftwaves on the RBM. We can relate the turbulence control parameter to the diamagnetic

parameter  $\alpha_d$ , which is defined by the ratio of characteristic scales of the drift wave and RBM:

$$\alpha_d = \frac{L_{dw}}{t_{dw}} \frac{t_{RBM}}{L_{RBM}}. \quad (\text{E.10})$$

Equation (E.10) describes the ratio of the characteristic velocity of the drift wave (the electron diamagnetic velocity) to the characteristic velocity  $L_{RBM}/t_{RBM}$  of the RBM. If  $\alpha_d > 1$  the structure disperses faster by diamagnetic propagation than it can grow. Therefore, it is called diamagnetic stabilization. The DALF equations are already normalized to the characteristic scales of the drift wave, spatial scales to  $\rho_s$  and times to  $\lambda_{pe}/c_s$ . Therefore, in DALF units  $L_{dw} = 1$  and  $t_{dw} = 1$ . The characteristic scales of the RBM are  $t_{RBM} = 1/\gamma_I$  and  $L_{RBM} = 1/k_{RBM}$ , where  $\gamma_I$  and  $k_{RBM}$  can be found in (B.5) and (B.12), respectively. Thus,

$$\alpha_{d,DALF} = k_{\parallel} \alpha_t^{-1/2} \omega_B^{-1/4}. \quad (\text{E.11})$$

This is equal to:

$$\alpha_{d,DALF} = \frac{1}{q_s R} \sqrt{\frac{1}{1 + \tau_i} \frac{m_i}{m_e} \frac{c_s R}{0.51 \nu_{ei}}} \left( \frac{R}{2\lambda_{\perp}} \right)^{1/4}. \quad (\text{E.12})$$

The diamagnetic stabilization can also be understood in terms of the cross-phase (E.6). At the RBM scale  $k_y = k_{RBM}$  the cross-phase becomes stabilized for:

$$\delta_e = \sqrt{\frac{\alpha_t \sqrt{\omega_B}}{k_{\parallel}^2}} < 1. \quad (\text{E.13})$$

In terms of  $\alpha_{d,DALF}$  (E.11) this provides the condition:

$$\alpha_{d,DALF} > 1, \quad (\text{E.14})$$

where both parameters  $\alpha_d$  and  $\alpha_t$  describe the transition between the drift wave and the RBM regime, they are different depending on the considered scale. The parameter  $\alpha_t$  describes when the characteristic scale of the drift wave ( $k_{\perp} \sim 1$ ) becomes interchange unstable, the parameter  $\alpha_d$  describes when the RBM becomes stabilized at its characteristic scale  $k_{\perp} \sim k_{RBM}$ . In L-mode, it is a very common situation that the RBM is not stabilized at its scale and the turbulence close to  $k_{\perp} \sim 1$  is drift-wave dominated. This regime of turbulence ( $\alpha_t < 1$ ,  $\alpha_d < 1$ ) is called drift-interchange turbulence. Pure drift-wave turbulence can be expected for  $\alpha_t \ll 1$  and  $\alpha_d \gg 1$ , pure RBM turbulence for  $\alpha_t \gg 1$  and  $\alpha_d \ll 1$ .

### Appendix F. Comparison to the density limit in Rogers, Drake and Zeiler

To see how the criterion  $k_{RBM} = k_{EM}$  is related to the original work in [10], we rewrite equation (3) in terms of  $\alpha_{MHD} = (1 + \tau_i) \hat{\beta} \omega_B$

$$\frac{\alpha_{MHD}}{\alpha_c} > \frac{(1 + \tau_i) \hat{\mu} \omega_B^{3/2}}{\alpha_t}. \quad (\text{F.1})$$

As the L-mode density limit occurs in the RBM regime, the diamagnetic parameter  $\alpha_d$  is the more natural parameter. We

replace  $\alpha_t$  by  $\alpha_d$  using  $\alpha_t = \alpha_c \omega_B^{-1/2} \alpha_{d,DALF}^{-2}$  (equation (E.11)) to obtain:

$$\alpha_{MHD} > (1 + \tau_i) \hat{\mu} \omega_B^2 \alpha_{d,DALF}^2 = (1 + \tau_i) 4 q_s^2 (m_e/m_i) \alpha_{d,DALF}^2. \quad (\text{F.2})$$

This is in full agreement with  $\alpha_{MHD} \sim \alpha_d^2$  being the boundary of the L-mode density limit as found in RDZ [10] at fixed gradient length scale, safety factor and ion to electron mass ratio. This relation is also in good agreement with the experimental observation previously reported in [12].

### Appendix G. Ideal-ballooning-mode limit

The maximum density in H-mode discharges is correlated with the ideal MHD ballooning stability limit at the separatrix [39]. In H-mode, the RBM can be expected to be suppressed by diamagnetic stabilization (see appendix E). However, if the plasma beta becomes sufficiently high to overcome the collisional dissipation, the overall system transits from resistive into ideal MHD conditions. This condition is considered here. We compare induction against collisional dissipation in equation (A.3):

$$\hat{\beta} \frac{\partial \tilde{J}_{\parallel}}{\partial t k_{\perp}^2} > C \tilde{J}_{\parallel}. \quad (\text{G.1})$$

We approximate the time derivative by the interchange growth rate  $d/dt \rightarrow \gamma = \sqrt{\omega_B}$

$$\hat{\beta} \frac{\gamma}{k_{\perp}^2} > C, \quad (\text{G.2})$$

and thus provide a selection rule for the wavenumber,

$$k_{\perp}^2 < \frac{\hat{\beta} \sqrt{\omega_B}}{C} \equiv k_{\text{ideal}}^2, \quad (\text{G.3})$$

which in terms of the turbulence control parameter  $\alpha_t$  is written as,

$$k_{\perp}^2 < \frac{(1 + \tau_i) \beta_e}{\frac{\alpha_t}{\omega_B^{3/2}} \frac{\lambda_{\perp}^2}{q_s^2 R^2}}. \quad (\text{G.4})$$

By inserting the RBM scale (equation (B.12)) into (G.4),

$$k_{\text{ideal}} = k_{RBM} \quad (\text{G.5})$$

the ideal ballooning limit (equation (C.5)) is recovered. Not only does the system transit into the MHD regime, but it is ideal MHD unstable. In this way, condition (G.4) allows us to observe the ideal ballooning stability limit in terms of  $\beta_e$  and  $\alpha_t$ .

### Appendix H. Turbulence suppression criterion for L–H

A criterion for triggering the L–H transition has been proposed in [49], which has been inspired by the Kim–Diamond model [50] attributing the L–H transition to the interaction between turbulence and flow shear, and by Scott [55] tracing the energy through turbulence. When the energy transferred from turbulence to the mean flow exceeds the drive of turbulence, the

turbulence can be considered to be suppressed. The energy transfer from turbulence to the mean flow is given by [60]:

$$\mathcal{P} = \langle \tilde{u}_x \tilde{u}_y \rangle \frac{\partial \langle u_y \rangle}{\partial x}, \quad (\text{H.1})$$

where  $\langle \tilde{u}_x \tilde{u}_y \rangle$  is the Reynolds stress and  $\frac{\partial \langle u_y \rangle}{\partial x}$  the flow shear. The energy input can be written by an effective growth rate  $\gamma_{\text{eff}}$  times the turbulence energy  $E_t$ . This yields a turbulence suppression criterion; turbulence collapses if the energy transfer from turbulence into the flow exceeds the energy input into turbulence [49]:

$$\frac{\mathcal{P}}{\gamma_{\text{eff}} E_t} > 1. \quad (\text{H.2})$$

The shear suppression criterion (equation (H.2)) has been experimentally confirmed by several experiments [49, 61–65] and reproduced by simulations as well [66–70].

In the following, the effective growth rate  $\gamma_{\text{eff}}$  and energy transfer  $\mathcal{P}$  will be related to the turbulence control parameter  $\alpha_t$ .

The energy input into turbulence is considered first. Motivated by [71], in addition to the kinetic energy  $E_{tk} = \frac{1}{2}(k\tilde{\phi})^2$ , we also take the free energy of both the electrons  $E_{te} = \frac{1}{2}\tilde{p}_e^2$  and the ions  $E_{ti} = \frac{1}{2}\tilde{p}_i^2$  into account, extending the approach reported earlier [49]. We assume  $\tilde{p}_e^2 \approx \tilde{p}_i^2 \approx \tilde{\phi}^2$ . Furthermore,  $k_x \approx k_y \approx k_\perp$  is assumed, thus  $k^2 = k_x^2 + k_y^2 \approx 2k_\perp^2$ . The total energy input into turbulence is  $\gamma_{\text{eff}} E_t = \gamma_e E_{tk} + \gamma_e E_{te} + \gamma_i E_{ti} = (\gamma_e \frac{1}{2}(1 + 2k_\perp^2) + \gamma_i \frac{1}{2})\tilde{\phi}^2$ .

Let us consider turbulence in the electron channel first. The parameter  $\alpha_t$  controls the transport by the cross-phase between electron pressure and potential fluctuations (approximated by an  $i\delta$  model, see equation (E.5)). The cross-phase also controls the growth of the electron pressure fluctuations given by  $\gamma = k_\perp \delta_e$  (see equation (A.2)). The relation of the cross-phase to  $\alpha_t$  can be found in equation (E.6). Overall, the growth rate of drift-interchange turbulence is approximated by:

$$\gamma_e = \alpha_t \frac{k_\perp^2}{k_\parallel^2}. \quad (\text{H.3})$$

Taken together, the electron contributions yield:

$$\gamma_e (E_{tk} + E_{te}) = \alpha_t \frac{k_\perp^2}{k_\parallel^2} \left( k_\perp^2 + \frac{1}{2} \right) \tilde{\phi}^2. \quad (\text{H.4})$$

The contribution of the ion heat flux is still missing. Ion temperature fluctuation does not take part in the parallel dynamics. The ITG is driven by the curvature similar to an interchange mode. We assume that the growth rate follows an ideal interchange instability:

$$\gamma_i = \sqrt{\omega_B \tau_i \Lambda_{pi}}. \quad (\text{H.5})$$

No critical gradient is taken into account and the ITG turbulence is assumed to be subcritically driven. The ion free energy is  $E_{ti} = \frac{1}{2}\tilde{p}_i^2 \approx \frac{1}{2}\tilde{\phi}^2$ . The energy input to the ion turbulence can be estimated by equation (H.5):

$$\gamma_i E_{ti} = \frac{1}{2} \sqrt{\tau_i \omega_B \Lambda_{pi}} \tilde{\phi}^2. \quad (\text{H.6})$$

In particular, at low  $\alpha_t$ , the energy input into the ion turbulence can be much larger than that into the electron turbulence.

Next, we estimate the energy transfer into the shear flow, which is ultimately responsible for the suppression of turbulence criterion (equation (H.2)). Weak or insufficient zonal flow activity at the L–H transition has been found in several experiments [27, 71–74]. This seems to be in contradiction to the suppression criterion (equation (H.2)), which has been explicitly formulated for zonal flows. We note that the suppression criterion (equation (H.2)) holds for any flow shear and applies to the background flow as well [75]. The energy transfer (equation (H.1)) can also be written as  $\mathcal{P} = \langle u_y \rangle \frac{\partial}{\partial x} \langle \tilde{u}_x \tilde{u}_y \rangle$ . The mean flow  $\langle u_y \rangle$  close to the L–H transition in ASDEX Upgrade is close to the ion diamagnetic flow in the electron diamagnetic (negative) direction [27], which in DALF units is given by  $\langle u_y \rangle = -\tau_i \Lambda_{pi} i$ . The complex number is added to allow for propagation. As  $\tilde{u}_x = -ik_y \tilde{\phi}$  and  $\tilde{u}_y = ik_x \tilde{\phi}$ , the Reynolds stress can be approximated by  $\frac{\partial}{\partial x} \langle \tilde{u}_x \tilde{u}_y \rangle \approx ik_x^2 k_y \tilde{\phi}^2$ . The energy transfer from turbulence to the mean flow is estimated as:

$$\mathcal{P} = k_x^2 k_y \tilde{\phi}^2 \tau_i \Lambda_{pi} \approx k_\perp^3 \tilde{\phi}^2 \tau_i \Lambda_{pi}. \quad (\text{H.7})$$

By tilting the turbulent structures the shear flow imposes a functional relationship between the radial  $k_x$  and binormal wavenumber  $k_y$ . However, as this relationship is not known, we also simplify here by setting  $k_\perp = k_x = k_y$ . This is consistent with the assumptions made previously when deriving equation (H.4).

The Reynolds stress drive is not efficient at low adiabaticity [47]. The eddies are tilted by the shear flow in the density. This tilt has to be transferred by the adiabatic response to the potential. In this model, this can be done by  $\tilde{p}_e = (1 - i\delta_e)/(1 + \delta_e^2)\tilde{\phi}$  (see equation (E.5)). This effect can be taken into account in the energy transfer rate (equation (H.7)):

$$\mathcal{P} = \frac{1}{(1 + \delta_e^2)} k_\perp^3 \tilde{\phi}^2 \tau_i \Lambda_{pi}. \quad (\text{H.8})$$

For parameters close to the L–H transition  $\delta_e^2 \ll 1$  (as  $\alpha_t < 1$ ,  $k_{EM} < 1$  and  $\alpha_c > 1$ ) this effect does not seem to have much impact. Therefore, we have neglected it so far. However, a possible shift to a lower cross-phase as observed in [76, 77] will make the energy transfer from turbulence to the shear flow more efficient. Approaching the H-mode by increasing the temperature leads to a reduced cross-phase between potential and electron pressure fluctuations. The cross-phase scales with  $\delta_e \sim \alpha_t$  (see equation (E.6)). In this way, the shear suppression criterion (equation (H.2)) can be fulfilled by both, making the energy transfer more efficient (increasing  $\mathcal{P}$ ) and reducing the effective growth rate of the electron thermal part of the turbulence  $\gamma_e$ . In this way, a cross-phase reduction can precede the amplitude suppression.

Inserting equations (H.4), (H.6) and (H.8) into the turbulence suppression criterion (H.2) provides:

$$\frac{k_\perp^3 \tau_i \Lambda_{pi}}{1 + \left( \frac{\alpha_t k_\perp}{k_\parallel^2} \right)^2} > \left( \alpha_t \frac{k_\perp^2}{k_\parallel^2} \left( k_\perp^2 + \frac{1}{2} \right) + \frac{1}{2} \sqrt{\omega_B \tau_i \Lambda_{pi}} \right). \quad (\text{H.9})$$



The term on the lhs is the stabilizing contribution by the flow shear. The strong  $k_{\perp}$ -dependence comes from the Reynolds stress, the dependence on  $\tau_i \Lambda_{pi}$  from the background ion flow. The terms on the rhs correspond to turbulence in the kinetic ( $E \times B$  drift), electron and ion channels. In the parameter region, the L–H transition take place in ASDEX Upgrade,  $\alpha_t$  is small and the ion channel dominates the turbulence growth.

Finally, we have to choose the characteristic wavenumbers  $k_{\perp}$  and  $k_{\parallel}$ . To include geometrical effects to some degree at least, we choose  $k_{\parallel} = \alpha_c$  according to the correspondence found in equation (C.5). We choose the characteristic electromagnetic wavenumber as the characteristic wavenumber  $k_{\perp} = k_{EM}$  (see equation (D.3)). An extended discussion on the choice of the characteristic wavenumber can be found in appendix I. By using these characteristic wavenumbers in the shear suppression criterion (H.9), the final criterion for the L–H transition is given by:

$$\frac{\alpha_c \sqrt{\frac{\beta_e}{\mu}} \tau_i \Lambda_{pi}}{1 + \left(\frac{\alpha_t}{\alpha_c}\right)^2 \frac{\beta_e}{\mu}} > \alpha_t \left(\frac{1}{2} + \frac{\beta_e}{\mu}\right) + \frac{1}{2} \frac{\alpha_c}{\frac{\beta_e}{\mu}} \sqrt{\omega_B \tau_i \Lambda_{pi}}. \quad (\text{H.10})$$

This criterion depends on a combination of dimensionless parameters describing plasma edge turbulence without any free adjustable parameter. These parameters are the plasma beta  $\beta_e$ , collisionality  $C$  (included by  $\alpha_t = (1 + \tau_i)C\omega_B$ ), magnetic curvature (included by  $\omega_B = 2\lambda_{pe}/R$ ), ion mass  $\mu = m_e/m_i$  and ion-to-electron temperature ratio  $\tau_i = T_i/\bar{Z}T_e$  and electron-to-ion pressure gradient ratio  $\Lambda_{pi}$ .

### Appendix I. Characteristic electromagnetic wavenumber for the L–H transition

For the construction of the plasma phase space of RDZ [10] it is argued that the electromagnetic fluctuations stabilize drift-wave turbulence. In this way, the turbulent transport could reduce with increasing  $\alpha_{MHD}$ . However, such a scaling is in contradiction with the results reported in [28, 58], showing that turbulent transport strongly increases with plasma beta. As discussed in appendix D, the nature of electromagnetic effects in plasma edge turbulence is a result of a complex interplay at different scales, which obviously cannot be captured in detail in a quasi-linear approach. To define a characteristic wavenumber, we assume drift waves in the domain  $k_{\perp}^2 < \frac{\beta_e}{\mu}$  being stabilized by electromagnetic effects. One might expect a lower turbulent drive in contradiction to [28, 58]. However, the characteristic wavenumber (equation (D.3)) increases with plasma beta and the turbulent transport increases with the characteristic wavenumber  $\Gamma_e \sim k_{\perp} \delta_e$ . Furthermore, the cross-phase also increases linearly with the wavenumber  $\delta_e \sim k_{\perp}$  at the same collisionality. Thereby, the electron transport increases linearly with the plasma beta  $\Gamma_e \sim \beta_e$  at the same collisionality. Without any flow shear, the electromagnetic stabilization of large-scale structures counterintuitively leads to enhanced transport. Besides this destabilizing effect, the shift towards higher wavenumbers introduces an additional

stabilizing effect, if the flow shear is taken into account. The stabilizing term representing shear suppression by energy transfer is proportional to the wavenumber. Turbulence suppression by energy transfer to the background shear flow is in fact induced by the enstrophy transfer between turbulence and the flow shear. The energy transfer is most efficient from small scales at  $k_{\perp} \sim 1$  [55, 78]. The closer the characteristic scale is to the drift-wave scale, the more efficient is the energy transfer. Both effects together are responsible for the occurrence of a minimum density to enter into the high-confinement regime. The ansatz  $k_{\perp} = k_{EM}$  used here is neither in contradiction to [10], where electromagnetic effects stabilize the drift-wave turbulence, nor to the results reported in [28, 58], showing that turbulent transport strongly increases with plasma beta.

### Appendix J. Experimental error estimation on strike line reconstruction

Experimental error estimation is performed for three systematic uncertainties acting on the reconstruction of the separatrix position. First, we allow for a variation in the power crossing the separatrix in the electron channel of  $90\% \pm 10\%$ . Second, the uncertainty of the subtracted radiation inside the separatrix is taken into account. For more details on the bolometer diagnostic, see [79]. In general, the reconstruction of  $Z_{eff}$  at the separatrix is difficult and not available for this large database. Therefore, we exclude all seeded discharges and execute dedicated discharges with good wall conditioning. The value for  $Z_{eff}$  corresponds to a boron concentration of  $1\% \pm 0.5\%$  and thus  $\bar{Z} = 1.04 \approx 1$ . The error bars are constructed by combining these uncertainties and denoted as lower (*l*), mean (*m*) and upper (*u*) values.

$$Z_{eff}^{l,m,u} = 1.24 \pm 0.13, \quad (\text{J.1})$$

$$P_{rad}^{l,m,u} = \int_{\rho=0}^{\rho=1.0 \pm 0.02} P_{rad}(\rho) d\rho, \quad (\text{J.2})$$

$$P_{sep}^{l,m,u} = 0.9 \pm 0.1 \cdot (P_{heat} - P_{rad}^{l,m,u}), \quad (\text{J.3})$$

$$T_{e,sep}^{l,m,u} \approx \left( \frac{7 P_{sep}^{l,m,u} \hat{q}_{cyl}^2 A}{16 \kappa_0^e \hat{\kappa} \lambda_q} \right)^{\frac{2}{7}} \quad \text{with } \lambda_q = \frac{2}{7} \lambda_T. \quad (\text{J.4})$$

The value for the parallel heat constant is calculated according to [8] and is written as:

$$\kappa_0^e = \frac{2600}{f_{\kappa,0}(Z_{eff})} \frac{W}{(\text{eV})^{\frac{7}{2}} m} \quad \text{with}, \quad (\text{J.5})$$

$$f_{\kappa,0}(Z_{eff}) = 0.672 + 0.076 Z_{eff}^{0.5} + 0.252 Z_{eff}. \quad (\text{J.6})$$

A minor difference is that the reference point in [12] is exactly the separatrix ( $\rho_{pol} = 1$ ). Here, the reference point is set to  $\rho_{pol} = 0.999$  and thus a confinement quantity, about 1 mm shifted inside w.r.t. the separatrix position (poloidally averaged).

## Appendix K. Estimation of plasma edge decay lengths

The applied scaling laws for the separatrix/SOL electron pressure, density and temperature decay lengths are:

$$\lambda_{pe}(m) = 1.2(1 + 3.6 \alpha_t^{1.9}) \rho_{s, pol}, \quad (K.1)$$

$$\lambda_{ne}(m) = 2.9(1 + 10.4 \alpha_t^{2.5}) \rho_{s, pol}, \quad (K.2)$$

$$\lambda_{Te}(m) = 2.1(1 + 2.1 \alpha_t^{1.7}) \rho_{s, pol}, \quad (K.3)$$

$$\rho_{s, pol} = \frac{\sqrt{m_D T_{sep}}}{e B_{pol}}. \quad (K.4)$$

Details on their estimation can be found in [12]. The reported error bars are tested and found to be entirely negligible for the conclusions drawn here.

The numerical value for the critical  $\alpha_{MHD}$  is calculated according to:

$$\alpha_c = \kappa_{geo}^{1.2} (1 + 1.5 \delta), \quad (K.5)$$

as applied in [39] and based on the work by Bernard [80]. The mean value for the database is  $\alpha_c = 2.37 \pm 0.14$ . The cylindrical safety factor is calculated according to:

$$\hat{q}_{cyl} = \frac{B_{tor}}{B_{pol}} \times \frac{\hat{\kappa}}{A} \quad \text{with} \quad B_{pol} = \frac{\mu_0 I_p}{2\pi a \hat{\kappa}}, \quad (K.6)$$

and

$$\hat{\kappa} = \sqrt{\frac{1 + \kappa_{geo}^2 (1 + 2\delta^2 - 1.2\delta^3)}{2}}. \quad (K.7)$$

## ORCID iDs

T. Eich  <https://orcid.org/0000-0003-3065-8420>

P. Manz  <https://orcid.org/0000-0002-5724-0174>

## References

- [1] Wagner F. 1997 *Plasma Phys. Control. Fusion* **39** A23
- [2] Greenwald M., Terry J.L., Wolfe S.M., Ejima S., Bell M.G., Kaye S.M. and Neilson G.H. 1988 *Nucl. Fusion* **28** 2199
- [3] Wagner F. et al 1982 *Phys. Rev. Lett.* **49** 1408
- [4] Greenwald M. 2002 *Plasma Phys. Control. Fusion* **44** R27
- [5] Saibene G. et al 1999 *Nucl. Fusion* **39** 1133
- [6] Mertens V. et al 2000 *Nucl. Fusion* **40** 1839
- [7] Suttrop W. et al 1999 *J. Nucl. Mater.* **266–269** 118
- [8] Goldston R.J., Reinke M.L. and Schwartz J.A. 2017 *Plasma Phys. Control. Fusion* **59** 055015
- [9] Kallenbach A., Sun H.J., Eich T., Carralero D., Hobirk J., Scarabosio A. and Siccinio M. 2018 *Plasma Phys. Control. Fusion* **60** 045006
- [10] Rogers B.N., Drake J.F. and Zeiler A. 1998 *Phys. Rev. Lett.* **81** 4396
- [11] Scott B.D. 2005 *Phys. Plasmas* **12** 062314
- [12] Eich T., Manz P., Goldston R.J., Hennequin P., David P., Faitsch M., Kurzan B., Sieglin B. and Wolfrum E. 2020 *Nucl. Fusion* **60** 056016
- [13] Lehnen M. et al 2013 *Nucl. Fusion* **53** 093007
- [14] Mertens V. et al 1997 *Nucl. Fusion* **37** 1607
- [15] Gates D.A., Brennan D.P., Delgado-Aparicio L. and White R.B. 2015 *Phys. Plasmas* **22** 060701
- [16] Labombard B., Boivin R.L., Greenwald M., Hughes J., Lipschultz B., Mossessian D., Pitcher C.S., Terry J.L. and Zweben S.J. 2001 *Phys. Plasmas* **8** 2107
- [17] Xu X.Q., Nevins W.M., Rognlén T.D., Bulmer R.H., Greenwald M., Mahdavi A., Pearlstein L.D. and Snyder P. 2003 *Phys. Plasmas* **10** 1773
- [18] Hong R. et al 2017 *Nucl. Fusion* **58** 016041
- [19] Giacomini M. and Ricci P. 2020 *J. Plasma Phys.* **86** 905860502
- [20] Rogers B.N. and Drake J.F. 1997 *Phys. Rev. Lett.* **79** 229
- [21] Halpern F.D., Jolliet S., Loizu J., Masetto A. and Ricci P. 2013 *Phys. Plasmas* **20** 052306
- [22] Carralero D. et al 2015 *Phys. Rev. Lett.* **115** 215002
- [23] Manz P., Carralero D., Birkenmeier G., Müller H.W., Müller S.H., Fuchert G., Scott B.D. and Stroth U. 2013 *Phys. Plasmas* **20** 102307
- [24] Sun H.J., Wolfrum E., Eich T., Kurzan B., Potzel S. and Stroth U. 2015 *Plasma Phys. Control. Fusion* **57** 125011
- [25] Sun H.J. et al 2017 *Plasma Phys. Control. Fusion* **59** 105010
- [26] Ricci P., Halpern F.D., Jolliet S., Loizu J., Masetto A., Fasoli A., Furno I. and Theiler C. 2012 *Plasma Phys. Control. Fusion* **54** 124047
- [27] Cavedon M., Pütterich T., Viezzer E., Birkenmeier G., Happel T., Laggner F.M., Manz P., Ryter F. and Stroth U. 2016 *Nucl. Fusion* **57** 014002
- [28] Scott B. 1997 *Plasma Phys. Control. Fusion* **39** 1635
- [29] Jenko F. and Scott B.D. 1999 *Phys. Plasmas* **6** 2705
- [30] Mandell N.R., Hakim A., Hammett G.W. and Francisquez M. 2020 *J. Plasma Phys.* **86** 905860109
- [31] Ryter F., Barrera Orte L., Kurzan B., McDermott R.M., Tardini G., Viezzer E., Bernert M. and Fischer R. 2014 *Nucl. Fusion* **54** 083003
- [32] Bilato R. et al 2020 *Nucl. Fusion* **60** 124003
- [33] Martin Y.R. et al 2008 *J. Phys.: Conf. Ser.* **123** 012033
- [34] Stangeby P. C. 2000 *The plasma boundary of magnetic fusion devices* (Boca Raton, FL: CRC Press)
- [35] Angioni C. and Sauter O. 2000 *Phys. Plasmas* **7** 1224
- [36] Viezzer E. et al 2013 *Nucl. Fusion* **53** 053005
- [37] Cavedon M. et al 2020 *Nucl. Fusion* **60** 066026
- [38] Sauter P. et al 2011 *Nucl. Fusion* **52** 012001
- [39] Eich T., Goldston R.J., Kallenbach A., Sieglin B. and Sun H.J. 2018 *Nucl. Fusion* **58** 034001
- [40] Stober J. et al 2000 *Plasma Phys. Control. Fusion* **42** A211
- [41] Ongena J. et al 2001 *Plasma Phys. Control. Fusion* **43** A11
- [42] Osborne T.H. et al 2000 *Plasma Phys. Control. Fusion* **42** A175
- [43] Osborne T.H. et al 2001 *J. Nucl. Mater.* **290–293** 1013
- [44] Leonard A.W., Jaervinen A.E., McLean A.G. and Scotti F. 2020 *J. Nucl. Mater. Energy* **25** 100869
- [45] Sun H.J. et al 2021 *Nucl. Fusion* **61** 066009
- [46] Sieglin B., Maraschek M., Kudlacek O., Gude A., Treutterer W., Kölbl M. and Lenz A. 2020 *Fusion Eng. Des.* **161** 111958
- [47] Schmid B. et al 2017 *Phys. Rev. Lett.* **118** 055001
- [48] Hajjar R.J., Diamond P.H. and Malkov M.A. 2018 *Phys. Plasmas* **25** 062306
- [49] Manz P. et al 2012 *Phys. Plasmas* **19** 072311
- [50] Kim E.-J. and Diamond P.H. 2003 *Phys. Rev. Lett.* **90** 185006
- [51] Bernert M. et al 2014 *Plasma Phys. Control. Fusion* **57** 014038
- [52] Brown A. and Goldston R.J. 2021 *J. Nucl. Mater. Energy* **27** 101002
- [53] Scott B. 1998 *Contrib. Plasma Phys.* **38** 171
- [54] Scott B. 1998 *Plasma Phys. Control. Fusion* **40** 823
- [55] Scott B.D. 2005 *New J. Phys.* **7** 92
- [56] McCarthy D.R., Guzdar P.N., Drake J.F., Antonsen T.M. and Hassam A.B. 1992 *Phys. Fluids B* **4** 1846
- [57] Zeiler A., Biskamp D., Drake J.F. and Guzdar P.N. 1996 *Phys. Plasmas* **3** 2951
- [58] Scott B.D. 2002 *New J. Phys.* **4** 52
- [59] Scott B.D. 2003 *Plasma Phys. Control. Fusion* **45** A385

- [60] Manz P., Xu M., Fedorczak N., Thakur S.C. and Tynan G.R. 2012 *Phys. Plasmas* **19** 012309
- [61] Tynan G.R. *et al* 2013 *Nucl. Fusion* **53** 073053
- [62] Yan X., Zheng J., Jiang X., Li M., Li M. and Wang Z. 2014 *Laser Phys. Lett.* **11** 125002
- [63] Shesterikov I. *et al* 2013 *Phys. Rev. Lett.* **111** 055006
- [64] Cziegler I., Tynan G.R., Diamond P.H., Hubbard A.E., Hughes J.W., Irby J. and Terry J.L. 2014 *Plasma Phys. Control. Fusion* **56** 075013
- [65] Cziegler I., Tynan G.R., Diamond P.H., Hubbard A.E., Hughes J.W., Irby J. and Terry J.L. 2015 *Nucl. Fusion* **55** 083007
- [66] Miki K. *et al* 2013 *Phys. Rev. Lett.* **110** 195002
- [67] Park G.Y., Kim S.S., Jhang H., Diamond P.H., Rhee T. and Xu X.Q. 2015 *Phys. Plasmas* **22** 032505
- [68] Li B., Wang X.Y., Sun C.K., Meng C., Zhou A. and Liu D. 2017 *Phys. Plasmas* **24** 055905
- [69] Chang C.S. *et al* 2017 *Phys. Rev. Lett.* **118** 175001
- [70] Ku S. *et al* 2018 *Phys. Plasmas* **25** 056107
- [71] Diallo A., Banerjee S., Zweben S.J. and Stoltzfus-Dueck T. 2017 *Nucl. Fusion* **57** 066050
- [72] Kobayashi T. *et al* 2013 *Phys. Rev. Lett.* **111** 035002
- [73] Cheng J. *et al* 2013 *Phys. Rev. Lett.* **110** 265002
- [74] Itoh K., Kobayashi T., Ido T., Itoh S.-I. and Kamiya K. 2015 *Plasma Phys. Control. Fusion* **57** 092001
- [75] Ullmann T., Schmid B., Manz P., Tovar G.E.M. and Ramisch M. 2021 *Phys. Plasmas* **28** 052502
- [76] Birkenmeier G., Ramisch M., Schmid B. and Stroth U. 2013 *Phys. Rev. Lett.* **110** 145004
- [77] Kobayashi T. *et al* 2017 *Sci. Rep.* **7** 14971
- [78] Manz P., Ramisch M. and Stroth U. 2009 *Phys. Rev. Lett.* **103** 165004
- [79] David P. *et al* 2021 *Nucl. Fusion* **61** 066025
- [80] Bernard L.C., Helton F.J., Moore R.W. and Todd T.N. 1983 *Nucl. Fusion* **23** 1475